ACS NANOSCIENCE Au
AN OPEN ACCESS JOURNAL OF THE AMERICAN CHEMICAL SOCIETY

pubs.acs.org/nanoau Review

# Electronic Quantum Materials Simulated with Artificial Model Lattices

Saoirsé E. Freeney, Marlou R. Slot, Thomas S. Gardenier, Ingmar Swart, and Daniel Vanmaekelbergh*

Cite This: *ACS Nanosci. Au* 2022, 2, 198–224 Read Online

ACCESS | Metrics & More | Article Recommendations

**ABSTRACT:** The band structure and electronic properties of a material are defined by the sort of elements, the atomic registry in the crystal, the dimensions, the presence of spin–orbit coupling, and the electronic interactions. In natural crystals, the interplay of these factors is difficult to unravel, since it is usually not possible to vary one of these factors in an independent way, keeping the others constant. In other words, a complete understanding of complex electronic materials remains challenging to date. The geometry of two- and one-dimensional crystals can be mimicked in artificial lattices. Moreover, geometries that do not exist in nature can be created for the sake of further insight. Such engineered artificial lattices can be better controlled and fine-tuned than natural crystals. This makes it easier to vary the lattice geometry, dimensions, spin–orbit coupling, and interactions independently from each other. Thus, engineering and characterization of artificial lattices can provide unique insights. In this Review, we focus on artificial lattices that are built atom-by-atom on atomically flat metals, using atomic manipulation in a scanning tunneling microscope. Cryogenic scanning tunneling microscopy allows for consecutive creation, microscopic characterization, and band-structure analysis by tunneling spectroscopy, amounting in the analogue quantum simulation of a given lattice type. We first review the physical elements of this method. We then discuss the creation and characterization of artificial atoms and molecules. For the lattices, we review works on honeycomb and Lieb lattices and lattices that result in crystalline topological insulators, such as the Kekulé and "breathing" kagome lattice. Geometric but nonperiodic structures such as electronic quasi-crystals and fractals are discussed as well. Finally, we consider the option to transfer the knowledge gained back to real materials, engineered by geometric patterning of semiconductor quantum wells.

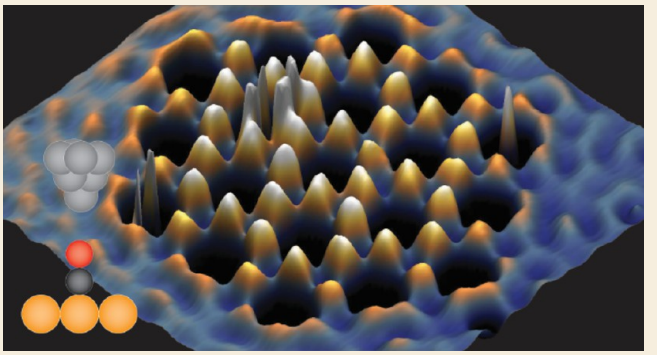

**KEYWORDS:** *quantum simulation, artificial lattices, Dirac bands, topology, scanning tunneling microscopy*



## 1. THE EMERGENCE OF ELECTRONIC QUANTUM MATERIALS

The field of (topological) electronic quantum materials is one of the major research directions in current solid-state physics, connecting theorists, solid state chemists, material scientists, and experimental physicists. This rapidly expanding field has its origin in several theoretical and experimental advancements starting in the 1980s, and it was boosted by the isolation and full electronic characterization of graphene.

Although the concept of a "quantum material" is not strictly defined (indeed, the electronic properties of all materials have a basis in quantum mechanics), some materials could be considered more "quantum" than others. In the last decades, a number of striking macroscopic physical phenomena have emerged that can most appropriately be explained by plain quantum physics.[1,2] Notoriously, two-dimensional electron gases exhibiting the quantum Hall[3] and fractional quantum Hall effects,[4] several types of (high-temperature) superconductors,[5−10] semiconductors with optoelectronic properties that depend strongly on the overall dimensionality of the crystal[11−13] (0D–2D), the nanogeometry,[14−21] and, more recently, the rapidly expanding field of topological quantum materials with electronic surface or edge states.[22−44] In the latter, the boundary states are protected by topology: (i) by valence/conduction band inversion due to strong spin–orbit effect (so-called quantum spin Hall insulators) or (ii) by certain crystal symmetries (topological crystalline insulators).

For electronic solids, the extended wave functions (Bloch states) and related band structure depend in an intricate way on (i) the atomic elements of the crystal defining atomic energy levels and strength of spin–orbit coupling or magnetic

Received: November 24, 2021
Revised: January 24, 2022
Accepted: January 28, 2022
Published: February 15, 2022

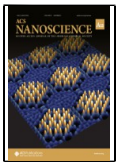





https://doi.org/10.1021/acsnanoscienceau.1c00054
*ACS Nanosci. Au* 2022, 2, 198–224

effects, (ii) the precise atomic registry defining the (anisotropic) electronic coupling, (iii) the overall dimensions of the system, i.e., in how many directions wave functions are confined, (iv) for 1D and 2D systems the superimposed nanogeometry, for instance, a two-dimensional electron gas molded in a Lieb, Kagome, or honeycomb geometry on the nanoscale, and (v) the presence of Coulomb or spin interactions between the quasi-particles. Theory has been dominant in the still young field of quantum materials. Several quantum phenomena of high potential interest have been put forward by theorists.[1,39,44−53] Experimental realizations often lag behind these theoretical predictions because a given "theoretically interesting" material has to be grown as a crystal with precise chemical composition and crystal structure, dimensionality, and nanogeometry. In addition, the material should not have (too many) defects or impurities. This requires advanced synthesis and structural characterization of the material down to the atomic level. Study of the electronic band structure requires incorporation of the material in an optical or electronic device for optical or electronic spectroscopy and/or transport measurements. For graphene, this cycle of material research could be completed due to graphene's intrinsic simplicity, simple growth and isolation, and chemical stability. Transport measurements in a magnetic field unambiguously demonstrated the anomalous quantum Hall effect, related to the electronic Dirac band structure of graphene.[54] Graphene can also be deposited or grown relatively easily on a flat metallic or insulator surface, allowing for atomic force[55−58] and scanning tunneling microscopy and spectroscopy.[58−65] An active and promising area of interest at present is the molecular synthesis of atomically precise ribbons of graphene[66] with well-defined arm-chair or zigzag edges. The measurement of their electronic band structure with scanning electron tunneling spectroscopy is directly linked to their atomic landscape, and reveals the direct influence of dimensions, edges and geometry on the electronic properties of a 2D crystal.[56,66−76]

The quantum materials that arrived on the scene after graphene were generally more complex. Strained 2D HgTe was the first material that was discovered to exhibit the famous quantum spin Hall effect,[34,36,77] the second important topologically protected electronic phase after the quantum Hall effect. The two-dimensional crystals of HgTe obtained a tweaked zinc blende crystal structure due to strain induced by epitaxy with CdTe. The strained zincblende structure and the strong intrinsic spin orbit coupling present in HgTe induces inversion of the conduction and valence bands. As a result, a topologically protected insulating gap arises in the HgTe crystal, with helical electronic states at the edges of the crystal. Here, helicity means that there is an edge state with the quasi-particle spin locked to its momentum in one direction, say $(E,k,\uparrow)$, and a second counterpropagating spin mode $(E,-k,\downarrow)$. The one-dimensional helical quantum channels support transport without dissipation: back scattering is impossible, except if there is a spin-flip. Later, 2D HgTe was also considered as a material basis for a nanoscale honeycomb structure. For this system, Dirac-type valence and conduction bands have been predicted. Due to the strong intrinsic spin−orbit coupling, a robust 30 meV band opening arises at the Dirac point, hosting quantum spin Hall edge states.[21] In this system, the quantum spin Hall effect is due to the honeycomb geometry combined with strong intrinsic spin−orbit coupling.[41,42] Two-dimensional crystals of HgTe with a honeycomb geometry on the nanoscale have not yet been experimentally realized.

## 2. ANALOGUE QUANTUM SIMULATIONS WITH ELECTRONIC ARTIFICIAL LATTICES AS MODEL SYSTEMS

The field of quantum materials is rapidly expanding with discoveries at the frontiers of science. However, all progress and in some cases lack of progress is directly related to reproducible material synthesis and the fabrication of clean samples for scanning tunneling microscopy and devices for transport analysis. Here, quantum simulations using artificial lattices, created atom-by-atom in a scanning tunneling microscope, and thus atomically precise, come on stage. Some materials might be so complex or difficult to fabricate that it is worth building an artificial analogue that mimics several of the essential elements of the original material and is thus described with a similar Hamiltonian. Artificial lattices provide more control and are often easier to characterize than complex real materials.[78] Quantum simulations have addressed questions in electronic material science,[79−85] fundamental physics,[86−90] and chemistry.[78,89,91] As far as we know, the first ideas on quantum simulation go back to Richard P. Feynman.[92,93] Furthermore, with his lecture "There is plenty of room at the bottom", he anticipated the creation of quantum architectures by control over individual atoms; nothing more than a futuristic concept at that time. These ideas have now been fully realized with cold atoms in optical lattices and with atomic manipulations in a scanning tunneling microscope.

The artificial atoms, molecules, and lattices that we will discuss in this review are electronic in nature and fabricated in a scanning tunneling microscope by atomic manipulation of adatoms (or CO molecules) on a flat metallic surface. We will outline the concept of a designed artificial electronic lattice, its physical elements, and its characterization. Briefly, artificial two-dimensional sites can be defined by arrays of adatoms or carbon monoxide molecules on well-defined positions on a metallic substrate. The surface state electrons are forced into artificial sites. These sites can be considered artificial atoms, be it in two dimensions. Artificial molecules and entire lattices, devoid of impurities, can be constructed from this type of artificial atom. With scanning tunneling spectroscopy, the local density of states (LDOS or electron probability density $|\varphi|^2(x,y)$) can be measured, from which the band structure is derived. This methodology can thus provide a one-on-one relationship between electronic band structure and the lattice geometry, a powerful tool to test concepts and theories. We remark here that artificial atoms, molecules, and lattices can also be engineered by assembling corral-type organic structures and periodic organic scaffolds to mold the two-dimensional electron gas present on the surface of noble metals.[94−96]

Artificial model systems are versatile. In addition to mimicking 2D materials on an atomic level, defects and impurities can be introduced and the consequences for the electronic band structure can be quantified. In an artificial lattice, it is also possible to change one parameter at a time, which is usually not the case in real materials. Furthermore, theories often use simplified assumptions; artificial lattices enable us to check the validity of these assumptions since they are based on experimental observations. For instance, band structure predictions are often based on tight-binding calculations based on nearest-neighbor hopping only. Measurements on artificial lattices have shown that next-nearest-


https://doi.org/10.1021/acsnanoscienceau.1c00054
ACS Nanosci. Au 2022, 2, 198−224

neighbor hopping may substantially change the predicted band structure, e.g., by showing that predicted flat-bands obtain a (weak) dispersion.[97]

A drawback of artificial lattices created with adatoms on a metallic surface is that surface-bulk scattering of the electrons results in a limited coherent lifetime of the surface states electrons, thus causing broadening of electronic resonances. This depends on the metal and its crystallography; for instance, on the Cu(111) surface, lifetime scattering results in broadening effects of about 24 meV at the band minimum at 4.6 K.[98] This value increases to about 80 meV in artificial lattices made from CO. In contrast, lifetime scattering on the Ag(111) surface is only about 6 meV at 4.6 K[98].

So far, electronic correlations, Cooper pair formation, and spin−orbit coupling have not been introduced in artificial electronic lattices, although they are essential physical elements of many real quantum materials and may result in topologically protected electronic phases.[22,99−103] These components are important next steps in the pursuit of the mastery of quantum materials. It is possible that a metallic substrate or adatoms of high atomic mass, such as thallium, lead, or bismuth, could induce spin−orbit coupling into the surface-state electronic gas.[104] Superconductive proximity from the underlying metal may induce electron pair formation in a surface state electron gas.[105−107] Coulomb interactions between the electrons are an essential element in many quantum materials. The artificial lattices reported so far have a high electron density and thus a strong screening of these interactions. To enable simulation of Coulomb interactions, electron-poor surface-states will be required for systems in which the density of the surface gas can be manipulated by an electrostatic gate. This stage has not been reached yet. So far, artificial lattices prepared on flat metallic surfaces are appropriate to simulate the effects of lattice geometry in the single-electron regime. Even with these limitations, interesting lattices with Dirac bands, flat bands, and topological edge states have been simulated in a very convincing way. Before we review these systems, we shortly discuss analogue quantum simulations with particles other than electrons.

## 3. QUANTUM SIMULATIONS WITH OTHER PARTICLES

A large variety of platforms are used for analogue quantum simulation, e.g., ultracold atoms, trapped ions, superconducting circuits, gated semiconductors, and optical lattices. The platform in which analogue quantum simulations have reached the most advanced stage is that of ultracold atoms caught in optical lattices.[79,84,108,109] Two-dimensional lattices with potential wells and barriers are created with crossing laser beams; they are loaded with ultracold atoms (bosons or Fermions) with a temperature in the nanokelvin regime.[110,111] The atomic occupation of each lattice site is measured by light scattering and monitored as a function of the on-site energies, tunneling barriers, lattice geometry, and external fields. The average occupation is usually smaller than one atom per lattice site. Although the lattice engineering, length scales, particles, and monitoring of the particle positions are completely different from those in electronic lattices, the class of physical questions that can be investigated is very similar. For instance, flat bands in the Lieb and honeycomb lattices have been simulated.[82,97,112,113] This has also been done with artificial electronic lattices. The advanced stage of cold-atom optical lattices has enabled the investigation of on-site interactions and spin−orbit coupling.[82,114−116]

A second material system that has proved successful in analogue quantum simulations is that of pillar arrays of III−V semiconductors. Each pillar contains a stacking of quantum wells and optical cavities to increase the interaction between a quantum-well exciton and its resonant photon. The resulting quasi-particle (or excitation) of interest is hence an exciton-polariton.[117] The geometry of the array of semiconductor pillars defines the lattice with lattice sites and hopping barriers for the exciton polaritons.[118−137] The de Broglie wavelength of exciton polaritons is large and is used to control hopping and interaction in the lattice. Exciton-polariton lattices are very powerful quantum simulators and could simulate the effects of lattice geometry on the band structure, from the single-particle regime[119,138−141] to that of (strong) interactions.[142−144] In the limit that exciton-polaritons are nearly photons, we deal with purely photonic lattices, which also have shown strong potential for quantum simulation.[131,145,146]

Quantum simulations with arrays of semiconductor quantum dots in which the electron occupation per quantum dot can be controlled by individual gates also allow for the study of many-body effects.[90,147−150] These arrays are most alike the artificial lattices on metallic surfaces that are presented below.

## 4. THE PHYSICAL ELEMENTS OF ARTIFICIAL LATTICES PREPARED IN A SCANNING TUNNELING MICROSCOPE

This section will describe the separate physical elements underlying the modeling of quantum materials with artificial electronic lattices. Each of these elements is the result of extensive theoretical and experimental research, work that in some cases has even resulted in a Nobel prize. We have chosen to construct a brief and comprehensive review that contains sufficient detail to understand the principles behind the creation and characterization of artificial electronic lattices in a scanning tunneling microscope and their characterization with scanning tunneling spectroscopy; these activities can be considered as attempts of "analogue quantum simulation" of real lattices with the same geometry.

### Scanning Tunneling Microscopy and Spectroscopy

After its invention,[151,152] scanning tunneling spectroscopy was rapidly developed as an accurate method to map the atomic structure of metallic surfaces and adsorbed flat molecules or two-dimensional systems. In brief, an electrically conductive tip is scanned over a metallic surface, with the tip in quantum mechanical tunneling contact with the surface. This means that the tip is within a nanometer of the metallic surface. A bias $V$ is applied between the tip electrode and the metallic substrate, inducing an electric field over the vacuum gap between the tip and the metal surface. This results in a controlled difference between the Fermi energy of the tip and that of the substrate, which constitutes the thermodynamic driving force for directed electron tunneling. The bias $V$ is defined as $eV = E_{F,tip} - E_{F,sample}$. The convention here is that, at positive bias, the Fermi level of the tip $E_{F,tip}$ is at higher energy than that of the sample, $E_{F,sample}$. When $V$ is different from zero, an electron tunnel current flows from the tip to the substrate, or vice versa, and this current (usually smaller than 1 nA) is measured in an external circuit. At positive bias, electrons can tunnel from the tip to the substrate. Quantum mechanical electron tunneling


https://doi.org/10.1021/acsnanoscienceau.1c00054
ACS Nanosci. Au 2022, 2, 198−224

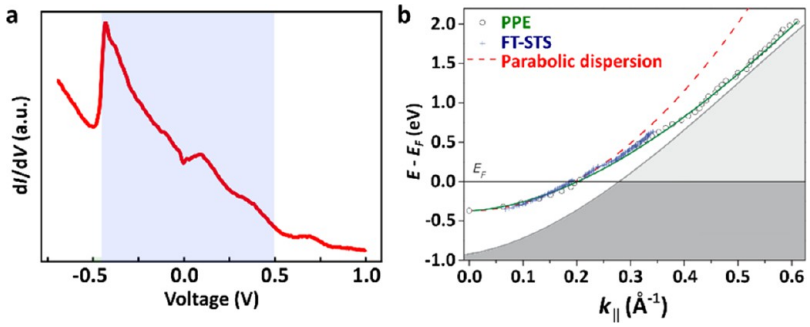


**Figure 1.** Two-dimensional electron gas residing on the surface of Cu(111). (a) Typical surface state band of a Cu(111) surface as characterized by scanning tunneling spectroscopy. The surface state sets on at $V = -0.45$ V. The shaded energy range between −0.45 and 0.5 V is suitable to localize electrons in artificial lattices. (b) Energy-wavevector dispersion of the Cu(111) surface state electrons presented in the gap above a filled bulk band (gray). The Fourier-transformed scanning tunneling spectroscopy data (blue) coincide with the results of photoemission spectroscopy (green) and follow a parabola in the energy range between −0.45 and 0.5 V. Reprinted with permission from ref 173. Copyright 2011 the American Physical Society.

between (the last atom on) the tip and the metal surface is roughly exponentially dependent on the tip−surface distance, which allows one to map the atomic periodicity of the metal surface, or to detect the presence of adatoms or molecules. In other words, a spatial map of the current variations at constant tip height (or more commonly, tip height at constant current) represents the atomic corrugation of the surface and highlights adsorbed species.[153]

The scanning tunneling microscope also allows one to perform powerful spectroscopy, providing the local electronic density of states, denoted as LDOS($E$,$x$,$y$). Briefly, the tip is positioned with atomic accuracy at a specific position ($x$,$y$) on the sample at a given and constant tip height. The bias $V$ between the tip electrode and the substrate is varied, and the tunnel current $I$ and conductance d$I$/d$V$ are measured as a function of the bias $V$; d$I$/d$V$ vs $V$ corresponds then to the LDOS($E$) at that position. To understand this, we consider a quantum mechanical system with discrete energy levels (e.g., an adatom, molecule, quantum dot) on the substrate surface with the tip placed above this system. When the bias is increased above zero, a tunnel current is detected when the Fermi-level of the tip becomes resonant with an empty energy level of the quantum system. Hence, the empty energy level is measured as a step in the ($I$,$V$) curve or as a peak in the d$I$/d$V$ vs $V$ plot. The next energy level is then detected as a second peak in the d$I$/d$V$ vs $V$ plot. The same holds when the bias is made negative, and the filled energy levels of the quantum system are detected by onsets of tunneling from the substrate to the tip. We conclude that the energy levels of quantum mechanical objects on a metallic surface can be measured by scanning tunneling spectroscopy.[154−165] Two remarks should be added: First, when an electron enters an adsorbed quantum system, it charges this object; this means that the resonance occurs at an energy equal to single-particle energy + the charging energy (also noted as self-energy). This charging energy can be expressed as $e^2/C$, with $C$ being the capacitance of the quantum object in the given tip/object/substrate double-barrier junction. If a second electron tunnels into the object before the first one has left, double charging occurs and the resonance bias $V$ for the second electron is increased by an amount equal to the Coulomb energy.[166] This means that, in principle, tunneling spectroscopy allows one to quantify the single-particle energy of the eigenstates, and the energy scale of Coulomb repulsion between the two (or more) electrons populating the quantum object as well.[161] In the literature, there is a vast number of reports on energy-level spectroscopy of metallic samples, adsorbed atoms, molecules, and extended lattices.

This Review focuses on the spectroscopy of artificial atoms and artificial lattices prepared directly on metallic surfaces by atomic manipulation in a scanning tunneling microscope (STM). The screening of the self-energy and electron−electron interactions within these systems is strong, and we can safely assume that the tunneling-resonances, discussed below, quantify the single-electron energy levels or dispersive bands of the system. Hence, the single-particle local density of states LDOS($E$) is measured at a certain position ($x$,$y$) by d$I$/d$V$ vs $V$. The magnitude of d$I$/d$V$ is proportional to the squared wave function of the eigenstate at given bias (given energy). In other words, a spatial map of d$I$/d$V$ at given bias $V$ reflects the energy-resolved local density of states LDOS($E$,$x$,$y$), also called the probability density $|\varphi(E,x,y)|^2$, of the system. Scanning tunneling microscopy, spectroscopy, and wave function mapping are appropriate tools in the study of artificial lattices.

## Metals with Surface State Two-Dimensional Electron Gases

In 1939, William Shockley published an influential work on the energy levels and bands related to the surfaces of three-dimensional metallic crystals.[167] This work commented on and incorporated earlier work of Tamm[168,169] and Goodwin.[170−172] The argumentation starts with a finite linear chain of quantum-mechanically coupled atoms. It is obvious that the potential energy landscape at both ends of the chain is different from the interior of the chain. The coupling of $N$ atoms in the chain results in $N$ energy levels that can form a dispersive band. Due to the deviating potential landscape of the ends of the chain, two of the $N$ energy levels can be energetically separated from the band. The two energy levels have a strong electron density localization over a few atoms at the ends of the chain. In the three-dimensional case, considering a crystal of $N \times N \times N$ atoms, on the order of $N^2$ levels are localized on surface atoms, and Shockley anticipated that these energy levels themselves can form a two-dimensional dispersion with in-plane wave vectors, separated from the bulk bands. Such a band thus contains electrons caught in a two-dimensional potential with free motion and wavevectors parallel to the surface, i.e., a two-dimensional electron gas. Surface bands of energy close to or overlapping with the bulk Fermi level are of particular importance.


https://doi.org/10.1021/acsnanoscienceau.1c00054
ACS Nanosci. Au 2022, 2, 198−224

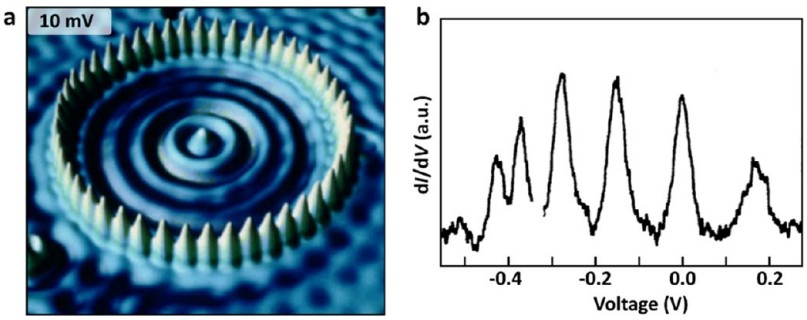


**Figure 2.** Quantum corral or artificial atom in two dimensions prepared on a Cu surface by atomic manipulation. (a) The quantum corral consists of 48 Fe atoms, positioned by atomic manipulation in a circle with a radius of 7.13 nm. The scanning tunneling spectroscopy $|\varphi(E,x,y)|^2$ map (wave function map) reveals the standing-wave pattern inside the corral at a bias of $V$ = 10 mV. Reprinted with permission from ref 341. Copyright 1999 the American Physical Society. (b) Tunneling conductance $dI/dV$ vs the bias $V$, acquired in the center of the corral, shows well-defined discrete energy levels, which can be considered as the eigenstates of the artificial atom. Reprinted with permission from ref 342. Copyright 1993 American Association for the Advancement of Science.

The surface-state band of a Cu(111) surface, characterized by scanning tunneling spectroscopy, was reported by the IBM Almaden group and confirmed by other experiments.[174−176] Figure 1 shows the results that were obtained. The surface state density sets on at an energy of −0.45 eV with respect to the Fermi-level, rises rapidly to a maximum, before slowly decaying to become negligible at 0.5 eV. With angle resolved photo emission spectroscopy (ARPES), the energy vs surface-parallel wavevector dispersion was determined, being nearly the same as that obtained with scanning tunneling spectroscopy.[175−177] The energy region between −0.45 and +0.5 eV will thus form *our working region of interest*; in this region, it is possible to confine the Cu (111) surface state electrons into artificial atomic sites and lattices (see below).

More generally, the energy vs wave vector dispersion relation of (electron-occupied) surface bands has been investigated extensively with scanning tunneling spectroscopy and Angle Resolved Photoemission Spectroscopy (ARPES), for several facets of noble metals.[155,178−191] Alternatively, the oscillatory LDOS patterns of surface waves at step edges or around scattering adatoms can be measured as a function of the bias, ultimately providing the dispersion relation and the effective surface electron mass, around $0.38m_o$ for Cu(111).[174,192] Furthermore, surface states can hybridize with the specific energy levels of an adatom, giving rise to an atom-localized electronic state that can often be distinguished from the two-dimensional surface band by scanning tunneling spectroscopy. For instance, a Cu adatom on a Cu(111) surface state gives rise to a localized state of energy just below the onset of the surface band itself.[193] By using atomic manipulation (see below), two-dimensional constructions of chains of Cu adatoms could be prepared. The energy levels and $dI/dV$ maps, proportional to the squared wave function, appear to be determined by the size and shape of the atomic chain.[194−198] In fact, these energy levels can be considered as arising from standing waves in a "molecule" of adatoms. In other words, "artificial atomic sites" emerge. Such architectures and others can be prepared on a sample surface with atomic accuracy, in a cryogenic scanning tunneling microscope. Atomic manipulation is the second physical element required to prepare and study artificial lattices.

## Atomic Manipulation of Atoms or Small Molecules Adsorbed on a Metal Surface

Adatoms and small molecules, such as carbon-monoxide CO, chemisorb on clean and flat metal terraces in such a way that a minimum-energy configuration is formed. Adatoms on, e.g., a (111) face of an fcc crystal typically take the trigonal valley between three atoms of the metal surface to maximize van der Waals and chemical interactions. CO forms an interesting exception to this, as on, e.g., a Cu(111) surface the carbon atom binds directly on top of a Cu atom.[199] If a metallic tip is brought closer to a chemisorbed CO or adatom, the adatom/tip attraction can become of the same order as the chemisorption energy, and an adatom might be transferred from the sample to the tip and placed on another well-defined position on the surface, i.e., vertical manipulation. In a subtler way, the tip can drag an adsorbate along the sample surface by applying a lateral force, position it, and then retract from the surface, i.e., horizontal/lateral manipulation. Atomic manipulation was developed in the beginning of the 1990s in the IBM Almaden group and extended by other groups; it was shown that noble gas atoms and transition metal adatoms could be positioned on a flat metallic surface.[192,200−208] Later, CO molecules chemisorbed with the C atom on top of the surface atoms could also be manipulated.[205,207] As CO molecules act as barriers for surface state electrons, they are appropriate for preparing artificial atomic sites, molecules, and lattices by confinement of these electrons in a limited surface area. It is precisely this confinement method that we have used extensively to prepare artificial lattices and even fractal structures (see below).

## Artificial Atoms and Molecules Defined by Adatoms

The orbitals of Cu adatoms can interact with the Cu(111) surface band, and form new states localized on the adatom.[193] This concept was soon extended to study adatom clusters with a well-defined shape and size. The eigenstate energy levels of these 2D architectures and maps of the squared standing wave function patterns[195,196] were obtained from scanning tunneling microscopy and spectroscopy. From this, it became clear that Cu adatom clusters form quantum boxes with atomic/molecular-type eigenstates. The interaction of these quantum eigenstates with (i) the surface band existing outside the system, and (ii) bulk bands of the Cu substrate results in a broadening of the states.[177] We remark here that, recently, In adatoms on a reconstructed (111) InAs surface have also been


https://doi.org/10.1021/acsnanoscienceau.1c00054
ACS Nanosci. Au 2022, 2, 198−224

used to engineer artificial molecular structures for which the molecular orbitals were characterized in terms of their energy and spatial extension.[209]

### Artificial Atoms, Molecules, and Lattices Defined by Vacancies in an Atomic Layer

Another way to prepare artificial systems is based on a CuCl monolayer crystal on a Cu(100) surface.[210] In this monolayer, Cl-vacancies can be manipulated and positioned at will using the STM tip. The Cl vacancies act as artificial atomic sites with a well-defined energy level, and ability to couple to identical neighboring artificial sites. Linear Su−Schrieffer−Heeger chains with topological end-states and a two-dimensional Lieb lattice were engineered by coupling of such vacancy sites.[83,211] Lattices made with this platform will be discussed below.

### Artificial Atoms, Molecules, and Lattices Defined by Confinement between Adatom or CO Barriers

The oscillatory patterns observed close to step edges and impurities indicate that surface-state electron waves, moving parallel with the surface, scatter with many sorts of adatoms. In a seminal work, corrals of such scatterers were prepared by atomic manipulation.[192] Inside the corral, the local LDOS shows a standing-wave pattern, which reflects the squared wave function of electron states confined into the corral, denoted as $|\varphi(E,x,y)|^2$ (see above and Figure 2). A sound quantum mechanical explanation of the energy levels and wave functions of such quantum corrals showed that they can be considered as artificial two-dimensional atomic sites.[212,213] In the next section, we present smaller quantum corrals as artificial atomic sites, which will then form the basis for artificial molecules and artificial lattices.

## 5. ARTIFICIAL ATOMS AND MOLECULES IN TWO DIMENSIONS

Here we discuss two-dimensional artificial atoms created by quantum corals formed by CO on Cu(111). We mention here that such corrals can also be formed by ring-shaped molecular architectures.[94]

### Artificial Atom: Wave Functions, Orbitals, and Energy Levels

We consider a corral defined by CO atoms on the Cu surface; see Figure 3. Each carbon monoxide molecule acts as a repulsive scatterer and defines an electrically repulsive potential of about 0.9 eV per CO.[214] In this way, a two-dimensional disk-shaped quantum box is defined, in which electrons are confined as standing waves.[174,192] In what follows, we will call such sites *artificial atoms*. An electron confined in such an artificial atom takes on quantized values of energy and angular momentum (for circular corrals).[213]

We model the disk-shaped quantum box by an origin (0,0) and a radius $a$. For simplicity, we will assume an infinite potential well around the circular artificial atom:

$$V(r) = 0 \text{ for } r < a, \qquad V(r \geq a) = +\infty \tag{1}$$

Using the polar coordinates $(r,\theta)$ and assuming that the radial and angular part of the wave functions can be separated, i.e., $\psi(r,\theta) = \Theta(\theta)R(r)$, the Schrödinger equation becomes

$$\frac{-\hbar^2}{2m}\left(\frac{\partial^2}{\partial^2 r} + \frac{1}{r}\frac{\partial}{\partial r} + \frac{1}{r^2}\frac{\partial^2}{\partial \theta^2}\right)R(r)\,\Theta(\theta) = ER(r)\,\Theta(\theta) \tag{2}$$

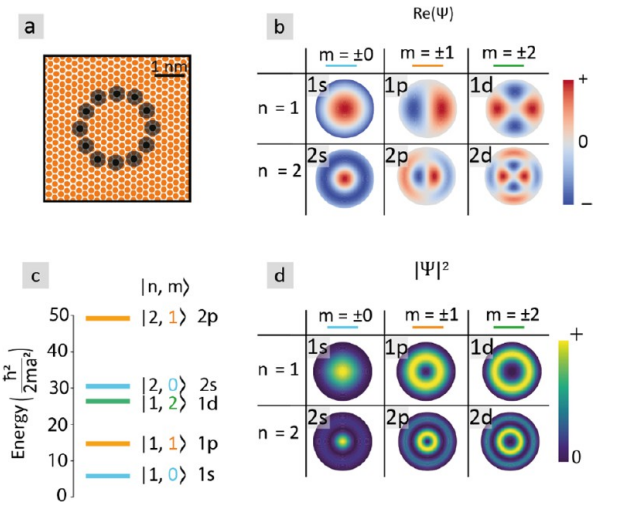


**Figure 3.** Orbitals of artificial atoms in two dimensions. (a) Artificial atom defined by a ring of electron-repulsive CO molecules (black) placed on specific positions on a Cu(111) surface (orange). (b) Analytical calculation of the real part of the wave functions labeled by their radial quantum number **n** and the angular momentum quantum number **m**. The $(n = 1, m = 0)$ orbital is equivalent to an s orbital. From the $(n = 1, m = -1)$ and $(n = 1, m = -1)$ orbitals, $p_x$ and $p_y$ orbitals can be constructed. (c) Energy scheme of the lowest energy levels labeled by $(n,m)$. (d) Squared modulus of the wave functions $|\varphi(E,x,y)|^2$, providing spatial maps of electron probability. Reproduced with permission from ref 343. Copyright 2020 SciPost Foundation.

The solutions are derived in the SI, section 1, and read:

$$\psi(r, \theta) = \frac{1}{\sqrt{2\pi}}R(n, m)e^{im\theta} \tag{3}$$

and

$$E(m, n) = \frac{\hbar^2}{2ma^2}a^2k(m, n)^2 \tag{4}$$

in which $R(n,m)$ is the two-dimensional *radial distribution function,* depending on the principal quantum number **n** and the angular quantum number **m**; it is a Bessel function of the first kind and of order **m**. The wave functions with quantum number **n** have **n** − 1 nodal circles in the quantum box. The function $e^{im\theta}$ describes the angular dependence of the wave function and depends only on the angular quantum number $m$, with $m = 0, \pm1, \pm2, \ldots$ and defines **m** nodal lines in the quantum box, or artificial atom. The energy levels and wave functions are presented in Figure 3. The two-dimensional wave functions bare a strong resemblance with the three-dimensional orbitals of real atoms. For instance, $(n = 1, m = 0)$ presents a 1s orbital and $(n = 1, m = +1)$, $(n = 1, m = -1)$ present wave functions that evolve clockwise and anticlockwise; from a linear combination of these two wave functions, $p_x$, $p_y$ orbitals can be formed. Furthermore, $(n = 1, m = +2)$, $(n = 1, m = -2)$ represent two in-plane d orbitals and $(n = 2, m = 0)$ has a nodal ring and corresponds to a 2s orbital. Please, notice that, in two-dimensional artificial molecules and lattices, the energy, symmetry, and sign of the lattice site orbitals are all important factors for the band structure.

### Artificial Atom: Experimental Realization and Characterization in an STM

We now present and discuss a circular artificial atom created on a Cu(111) surface; see Figure 4. Figure 4a shows the


https://doi.org/10.1021/acsnanoscienceau.1c00054
ACS Nanosci. Au 2022, 2, 198−224

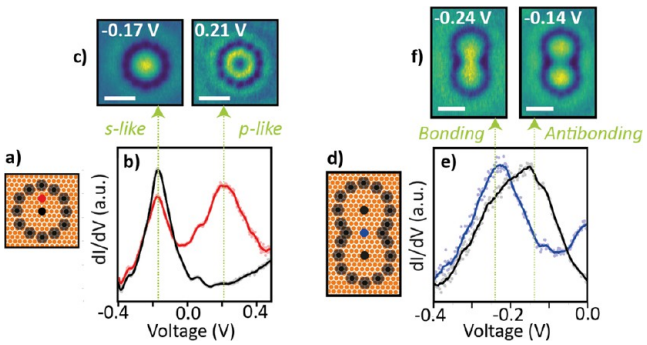


**Figure 4.** From artificial atoms to artificial molecules. (a) Schemes of the artificial atom and (d) artificial diatomic molecule. The dark dots represent CO molecules, and the orange dots represent the Cu(111) surface atoms. The positions on which the spectra were taken are marked in (a) black and red, and (d) black and blue. (b,e) d$I$/d$V$ spectra averaged over several measurements on each position and divided by the average bare Cu(111) spectrum acquired with the same tip. The light-colored dots represent this data. The continuous lines represent the moving average. (c) Differential conductance maps of the artificial atom showing the m = 0, $n$ = 1 (1s) and the $m$ = 1 or −1 (in-plane 1p) states at −0.17 and 0.21 V, respectively. (f) Differential conductance maps of the artificial dimer showing the bonding and antibonding combinations of two 1s orbitals at −0.24 and −0.12 V, respectively. Reproduced with permission from ref 343. Copyright 2020 SciPost Foundation.

schematic of a circular corral. d$I$/d$V$ vs $V$ (corresponding to the LDOS) spectra were acquired at the positions marked at the center and close to the boundary; see Figure 4b. The spectrum taken in the center shows a resonance at −0.17 V, while the one taken off-center shows an additional peak at 0.21 V. The maps of (d$I$/d$V$)($x$,$y$) (Figure 4c) show that the two resonances correspond to the ($n$ = 1, $m$ = 0), and ($n$ = 1, $m$ = −1), ($n$ = 1, $m$ = +1) states. The images are reminiscent of the probability density of s orbitals and degenerate p orbitals, respectively. Consequently, these states will be referred to as s-like and p-like states.

### Artificial Dimer-type Molecules: Experimental Realization and Characterization in an STM

The analogy of a quantum corral to an atom can be extended further: two corrals can be coupled together to form a dimer, resulting in an interaction between the on-site orbitals to form bonding and antibonding molecular orbitals. In a dimer, there is an increased probability density in between the two nuclei at the energy of the bonding state. The reverse is true for the antibonding orbital; in this case, a node exists between the corrals. The energies of bonding and antibonding orbitals are observed by measuring d$I$/d$V$ spectra at different positions in the artificial dimer; see Figure 4d. A spectrum in the region between the two sites shows a peak at −0.24 V corresponding to the bonding orbital. The antibonding state can be detected in the center of the two atoms at −0.14 V. Figure 4f shows differential conductance maps at the energies of the bonding and antibonding orbitals, respectively. This concept of coupling quantum corrals is the basis behind the construction of artificial electronic lattices, as was first demonstrated in a seminal study of an artificial honeycomb lattice (coined "molecular graphene".[215]

## 6. SIMULATION OF AN ELECTRONIC LIEB LATTICE

### General

The geometry of the Lieb lattice is well-known from the $AX_2$ planes in the 3D $ABX_3$ perovskite structure, such as the superconducting $CuO_2$ planes in cuprate high-temperature superconductors.[216] However, the geometry does not exist as such in a natural 2D material, making the electronic Lieb lattice an ideal candidate for analogue quantum simulation (see below). The Lieb lattice is a depleted square lattice, consisting of three (artificial) atoms per unit cell: two edge sites (red), connected to two nearest neighbors, and one corner site (blue) with four nearest neighbors[216,217] (see Figure 5a). The Lieb lattice can alternatively be defined as the split graph of the square lattice.[218] The three-atom basis gives rise to three s orbital bands. Two bands converge to a Dirac cone at the

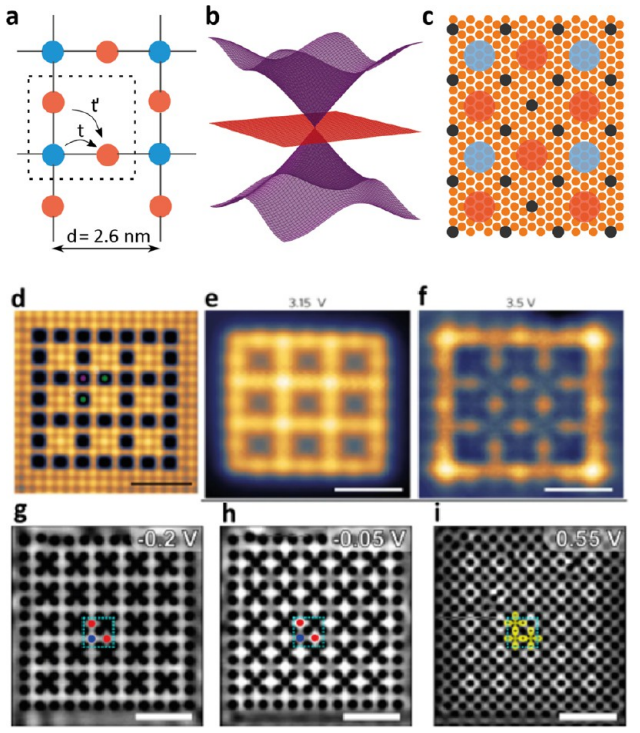


**Figure 5.** Quantum simulation of the Lieb lattice in a scanning tunneling microscope. (a) Schematic of the Lieb lattice. The unit cell (dashed contour) contains two edge sites (red) and one corner site (blue). (b) Band structure at the corner of the Brillouin zone of an ideal s orbital Lieb lattice, comprising a Dirac cone (purple) and flat band (red). (c) Configuration of CO molecules (black) on Cu(111) (orange background) to confine the Cu surface-state electrons into the Lieb geometry. (d) Configuration of chlorine vacancies (black) in a chlorine monolayer on Cu(100) (orange), coupled to a Lieb lattice. (e,f) Characterization of the Lieb lattice of chlorine vacancies, Figure 5d: (e) Wave function map at $V$ = 3.15 V, corresponding to the energy of the lowest Dirac band. (f) Wave function map at $V$ = 3.5 V, the flat band energy, showing a high LDOS at the edge sites of each unit cell. (g−j) Wave function maps for the Lieb lattice constructed with CO molecules on Cu, Figure 6c: (g) Wave function map at $V$ = −0.2 V, corresponding to the energy of the lowest Dirac band. (h) Wave function map at $V$ = −0.05 V, the flat band energy, showing a high LDOS at the edge sites of each unit cell. (i) Wave function map at $V$ = +0.55 V, showing the coupling of in-plane p orbitals in the Lieb lattice. Panels (a)−(c) and (g−i) are adapted with permission from ref 214. Copyright 201Springer Nature. Panels (d)−(f) are adapted with permission from ref 211. Copyright 2017 Springer Nature.


https://doi.org/10.1021/acsnanoscienceau.1c00054
ACS Nanosci. Au 2022, 2, 198−224

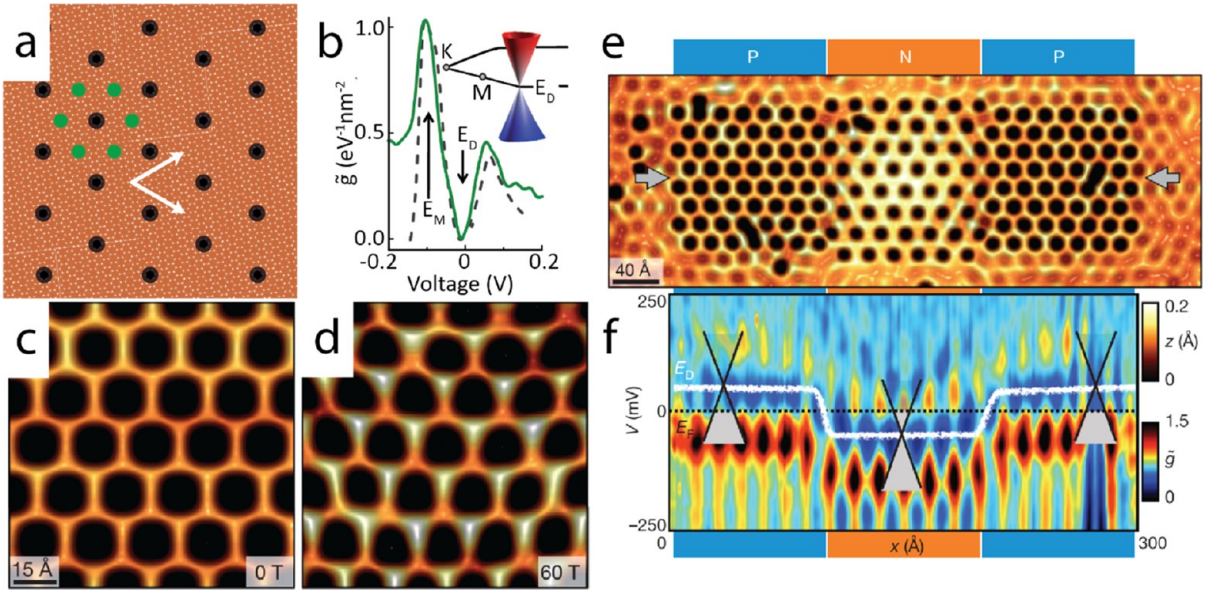


**Figure 6.** Design and realization of the first quantum simulation of a honeycomb lattice, "molecular graphene". (a) Schematic overview of the placement of the electron repelling CO molecules (black) on a Cu(111) substrate (copper), as performed by Gomes et al. The lattice vector is 1.92 nm. The green circles indicate the lattice sites of the honeycomb lattice. (b) Measurement of LDOS(E) as a function of the bias, showing the Dirac cone with the Dirac point indicated by $E_D$. The spectrum is an average of the positions indicated by green circles in (a). (c) Scanning tunneling microscope image of the artificial lattice with a high LDOS($E$,$x$,$y$) in yellow indicating the high electron probability in the honeycomb network. (d) Scanning tunneling microscope image of the stretched artificial lattice simulating a 60 T field. The LDOS is higher at one sublattice (bright sites) compared to the other sublattice (darker sites). (e) Scanning tunneling microscope image of adjoined honeycomb lattices with different lattice spacing (1.78 and 2.04 nm, respectively) forming a p−n−p junction. (f) Contour plot of the LDOS(E) taken along the center line of the p−n−p junction indicated by the arrows in (e). The dashed line at 0 mV marks $E_F$. The Dirac point (low electron density) is shown by the white line. Reprinted with permission from ref 215. Copyright 2012 Springer Nature.

Brillouin zone corners; the Dirac cone is intersected by a flat band (see Figure 5b). Similar to graphene, the linear dispersion in the Dirac cone leads to massless electrons which can propagate in the lattice at a constant velocity. In contrast, the electrons in the flat band are localized on the edge sites of each unit cell. Generally, the realization of a flat band is particularly interesting for the investigation of electron−electron interactions,[219−222] the quantum spin Hall effect,[134,216,223] and superconductivity.[106] An optical equivalent of the Lieb lattice was theoretically proposed[113,224] and subsequently realized in bosonic and Fermionic cold-atom lattices.[225,226] Moreover, photonic Lieb lattices were realized and the band structure was mapped.[135,219,220,222,227,228] Recently, exciton-polaritons[122,229] were studied in a Lieb geometry.

## Simulation of the Electronic Lieb Lattice

The *electronic* Lieb lattice was realized via two approaches: chlorine vacancies and CO on Cu(111). Drost et al. manipulated chlorine vacancies in a chlorine monolayer on Cu(100).[211] The approach was originally presented in the seminal work performed in the group of Otte.[83] A Lieb lattice of 3 × 3 unit cells with Cl-vacancies as artificial atoms was created, see Figure 5d. Differential-conductance spectra and maps showed the bottom Dirac band and the edge-localized flat band, corroborating the main characteristic features of the Lieb lattice (Figure 5e,f). An advantage of this approach is that the direct lattice is patterned, in contrast to the inverse geometry required for the CO-on-Cu(111) platform. Moreover, the Cl-vacancy platform is ideal for $C_4$-symmetric lattices. A disadvantage is that the on-site energy of the vacancy states is close to the Cl-conduction band, leading to a limited accessible energy range. As a consequence, the Dirac band above the flat band could not be resolved.

In the work of Slot et al.,[214] the CO-on-Cu(111) platform was used. The Lieb lattice is $C_4$-symmetric, which means that the lattice is not entirely compatible with the underlying Cu(111) lattice. However, since the artificial atoms formed by COs on top of the Cu atoms comprise many Cu atoms, good approximations to the Lieb lattice can be prepared, even on a hexagonal Cu(111) surface.[214,216,217,230,231] Since the Lieb lattice has no dual lattice, the inverse lattice was defined using crosses of five CO molecules, as indicated in Figure 5c. The unit cell was chosen such that the on-site energy was near the Fermi energy and the anisotropy of the $C_4$-symmetric Lieb lattice on the triangular Cu(111) background was minimized. Scanning tunneling spectroscopy resolved the bottom and top Dirac bands and a quasi-flat band. Furthermore, LDOS maps showed the localization of the Dirac bands on both the corner and edge sites (Figure 5g) while the flat band resides on the edge sites only (Figure 5h). The second band (supposedly flat) has acquired a dispersion due to a substantial next-nearest-neighbor hopping and coupling with higher-energy bands.

At energies above the three lowest bands, p orbital bands were observed (see Figure 5i). We should remark here that p orbital bands were first established in cold-atom lattices.[108,232] More recently, p orbital honeycomb and Lieb lattices were realized with photonic- and exciton-polariton excitations.[122,229,233] The $C_4$-symmetric Lieb lattice is a suitable candidate to describe p orbitals in a convenient $p_x$ and $p_y$ orbital basis.[234] Motivated by the higher-energy bands observed in the initial Lieb lattice, in Slot et al.,[234] the artificial-atom sites were enlarged in order to decrease the on-site energy and thus shift the p orbitals down to the


https://doi.org/10.1021/acsnanoscienceau.1c00054
ACS Nanosci. Au 2022, 2, 198−224

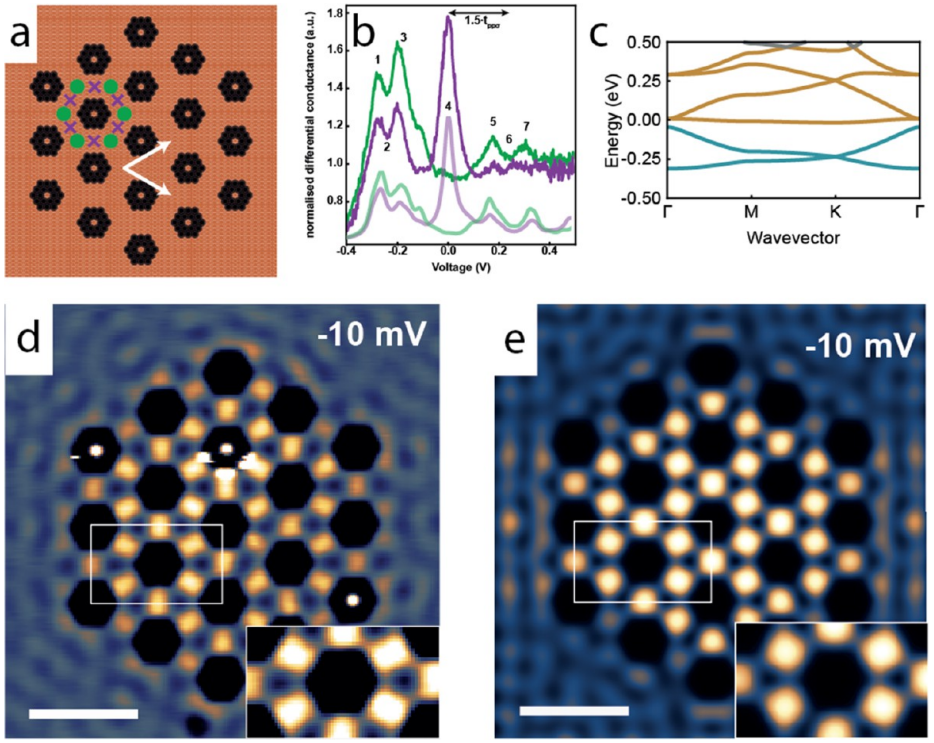


**Figure 7.** Design and realization of an artificial electronic honeycomb lattice with a separated s and p orbital Dirac cone and p orbital flat band. (a) Schematic overview of the placement of the electron repelling double-ringed CO rosettes (black) on a Cu(111) substrate (copper), as performed by Gardenier et al. The lattice vector is 3.58 nm, corresponding to 14 Cu atoms. The green dots indicate the positions of the honeycomb lattice sites; the violet crosses indicate the bridge positions between the lattice sites. (b) Experimental (dark) and theoretical (light) LDOS($E$) taken on the lattice sites (green) and on the bridge sites (purple). 1−3 reflect the first s orbital Dirac cone, with 1,3 being the M points and 2 being the Dirac point; 4 shows the flat-band due to interference of in-plane p orbitals with strong intensity on the bridge sites; 5−7 show the second Dirac cone due to the p orbitals. (c) Corresponding band structure for the design in (a) calculated by the muffin-tin approximation. The band structure reflects separated s (blue) and p (orange) orbital bands. (d,e) Wave function maps at the energy of the flat-band showing the nearly zero electron probability on the lattice sites (dark blue) and very large probability on the bridge sites (yellow) indicative for a p orbital band. (d) Experimental LDOS($x$,$y$) map and (e) muffin-tin calculation at the same energy. The black hexagons are the CO-rosettes. Reprinted from ref 260. Copyright 2020 American Chemical Society.

appropriate energy range $-0.45 < E < 0.5$ eV. LDOS maps displayed nodes on the artificial-atom sites and a finite DOS between the sites, characteristic for the low $p_x$ and $p_y$ orbital bands.[234] In addition, the on-site energies of the $p_x$ and $p_y$ orbitals were tuned separately by creating an asymmetric Lieb lattice, breaking the spectral degeneracy of the $p_x$ and $p_y$ orbital bands.

The work on s and p orbitals in the Lieb lattice established that the orbital degree of freedom is among the parameters that can be tuned in electronic lattices realized using CO on Cu(111). Orbital degree of freedom plays a crucial role in the creation of generic honeycomb lattices with separated s and p orbital bands, discussed in the next section.

## 7. SIMULATION OF A HONEYCOMB LATTICE WITH ORBITAL DEGREES OF FREEDOM

### General

The honeycomb lattice consists of two interpenetrated trigonal lattices with equivalent sites. Its unit cell consists of two sites (A and B) and thus a site of each trigonal sublattice. The coupling between nearest neighbor A and B sites in this geometry results in a linearly dispersed relation between energy and momentum in the regions around the K, K' points of the Brillouin zone (see Figure 6).[235] In the *generic* honeycomb system, in which each atomic site has an s orbital sufficiently separated in energy from the in-plane ($p_x$, $p_y$) orbitals, Dirac cones can be formed by coupling of the s orbitals, separately from the in-plane p orbitals.[49,236] The two orthogonal ($p_x$, $p_y$) orbitals cannot form conventional bonding−antibonding combinations; instead, their interaction gives rise to complex interference patterns. As a result, the four in-plane p bands consist of a nondispersive flat band, followed by two dispersive bands forming a Dirac cone at higher energy, followed by another flat band (see Figure 7). Since the kinetic energy is quenched in the flat bands, interactions form the dominant energy scale. It has been predicted that this will lead to new quantum phases, such as the p band quantum (spin) Hall effect, unconventional superconductivity and Wigner crystals.[49] The physics of in-plane p orbitals has been studied with ultracold atoms in optical lattices,[236−238] light in photonic systems,[233] and exciton-polaritons in a semiconductor pillar array.[122,138]

Natural atomic monolayer materials with honeycomb geometry include graphene, silicene, and germanene.[235,239−246] In graphene, the most studied electronic honeycomb lattice, the s and in-plane $p_x$, $p_y$ orbitals of the carbon atoms hybridize and form $sp_2$ electronic bands, with the lower one being completely filled.[235] This filled band leads to a very strong in-plane bonding between the carbon atoms, giving graphene its mechanical strength, but the band is far below the Fermi level and thus not electronically active. The remaining $p_z$ orbitals


https://doi.org/10.1021/acsnanoscienceau.1c00054
ACS Nanosci. Au 2022, 2, 198−224

(perpendicular to the graphene plane) form $\pi$ bonds, resulting in two bands touching at the (K, K') Dirac points at which the Fermi energy is situated. The linear energy-wave vector dispersion (Dirac cone) around the (K, K') points is responsible for the exciting electronic properties of graphene.

Solid-state electronic honeycomb systems can be realized in two-dimensional semiconductor materials by lithographic etching, giving access to genuine honeycomb semiconductors, hosting Dirac-type electrons and holes.[14−18,20,21,108,247−254] Alternatively, the self-assembly and epitaxial connection of nanocrystals at an interface has resulted in honeycomb semiconductors of II−VI materials.[255−259] The creation of 2D semiconductors with honeycomb nanogeometry with minimum disorder and the study of the optoelectronic properties is currently performed in several groups worldwide. We will discuss this in the outlook section of this work. First, we describe analogue quantum simulations of electronic honeycomb systems in detail.

## Simulation of "Molecular Graphene" by the Group of H. Manoharan[108,215]

An artificial honeycomb lattice engineered by manipulation of CO molecules on a Cu(111) surface in a scanning tunneling microscope was reported years ago; the lattice was coined "molecular graphene". This groundbreaking work showed the full potential of quantum simulations with artificial lattices prepared in a scanning tunneling microscope. First, a graphene-type honeycomb lattice with a single Dirac cone was created (Figure 6a and b). Second, by changing the size of the artificial atomic sites, the intrinsic Fermi level (at the Dirac point) could be changed; the epitaxial connection between two domains with a different intrinsic Fermi level results in electronic equilibrium, simulating a "p−n" junction, as for real materials (Figure 6e and f). Third, it was shown that deformations of the lattice are equivalent to a strong pseudomagnetic field (Figure 6c and d).

Figure 6a presents the design used in the Manoharan group; a hexagonal array of single CO scatterers (black dots) was prepared by atomic manipulation; this results in lattice vectors of 1.92 nm, hence considerably larger than that in real graphene. Figure 6e shows a scanning tunneling microscopy image, in which a honeycomb network of high electron probability can clearly be seen. Scanning tunneling spectroscopy (Figure 6b) revealed the local density of states (LDOS) corresponding to a single Dirac cone (indicated by $E_D$). The width between the two maxima around the Dirac point, i.e., the two M-points, is 180 meV, resulting in a hopping value of about 90 meV. From the steepness of the linear dispersion $E(k) = \hbar v_F k$, the group velocity (Fermi velocity) of the electrons is found to be $2.5 \times 10^5$ m/s, considerably smaller than in graphene.

Increasing (decreasing) the lattice spacing lowers (raises) the energy levels and the position of the Dirac cone. This can be seen in Figure 6e and f. The region labeled "p" is a honeycomb lattice with a smaller lattice spacing than that in panels (a) and (b), thereby confining the surface state electrons to a smaller area and raising the energy levels. The Dirac point is therefore situated above the Fermi energy $E_F$, resulting in a lattice with fewer electrons, i.e., a p-doped system. The opposite occurs when the lattice spacing is increased (labeled by "n"). Here, the Dirac cone is shifted to lower energies leading to electrons filling the upper band as well, i.e., a n-doped system. Attaching both systems to each other gives a p−n−p junction. Figure 6f shows the nearly instantaneous jump in energy of the Dirac cone position when going from one lattice type to the other.

Perhaps the most compelling highlight of this work is the deformation of the lattice by triaxial strain creating a pseudomagnetic field (gauge field) up to 60 T. The effect of the strain on the electron localization is visualized in Figure 6d, showing the difference between sublattice A and B at a pseudomagnetic field of 60 T. The spin symmetry of the sublattices has been broken; a zeroth order Landau state emerges on sublattice A; sublattice B sites show a Landau gap that gives mass (widens the gap at the Dirac point) to the Dirac electrons with pseudospin B.

It was not entirely clear which type of atomic site orbitals were involved in the formation of the Dirac bands. Calculations by Wang et al.[251] show that, for the design presented in Figure 6a, hybridization between the s and in plane ($p_x$,$p_y$) orbitals occurs, very similar to the case of real graphene. Below, it is shown that, by playing with the size of the artificial atomic sites and thus the on-site energy of the s and ($p_x$, $p_y$) orbitals, hybridization can be avoided to a large extent, resulting in a band scheme in which s orbital bands are separated from p orbital bands.

## Simulation of the Generic Electronic Honeycomb Lattice with Separated s and p Orbital Bands

Gardenier et al. extended the quantum simulation of electronic honeycomb lattices with designs that show separated s and p orbital Dirac bands, and, as a result, unclouded p orbital physics (see above).[260] The electronic bands can only be observed if they emerge in the energy window of the Cu(111) surface state, i.e. between −0.45 and +0.5 eV with respect to the copper Fermi level. Assisted by theory, Gardenier et al., tailored the energy of the s- and p orbital bands within this energy window by adjusting the lattice vector. As mentioned previously, a larger lattice vector causes the electronic states to drop in energy. Moreover, by using double-ringed rosettes of CO molecules, instead of a single CO molecule, the degree of quantum confinement and the coupling between the sites could be tuned. The final design is shown in Figure 7a.

The electronic band structure of this lattice is shown in Figure 7c. It was calculated by solving the Schrödinger equation with a muffin-tin potential accounting for the rosettes of CO molecules as repulsive scatterers. In addition, the muffin-tin band structure was fitted with a tight-binding model based on artificial atomic sites in a honeycomb lattice; each atomic site has one s orbital and two in-plane p orbitals, and s−s, s−p, and p−p hopping is allowed between neighboring sites. The band structure shows the p orbital flat band and Dirac cone, well separated in energy from the lower s Dirac cone. The four p orbital bands (orange) contain a (nearly) flat band and two dispersive bands forming a Dirac cone. Above these bands, hybridization becomes important. The muffin-tin calculations could also accurately reproduce the experimental results of a single s orbital Dirac cone in the LDOS(E) spectrum by Gomes et al. (see Figure 6b). This indicates that this approach is an appropriate electronic quantum simulator for the study of the in-plane p orbital physics.

The LDOS($E$) spectra on the on-site (green) and bridge site (purple) positions are presented in Figure 7b; they should be compared with the theoretical muffin-tin spectra, plotted in lighter colors below the experimental data. The first double peak (peaks 1 and 3) corresponds to two s orbital bands


https://doi.org/10.1021/acsnanoscienceau.1c00054
ACS Nanosci. Au 2022, 2, 198−224

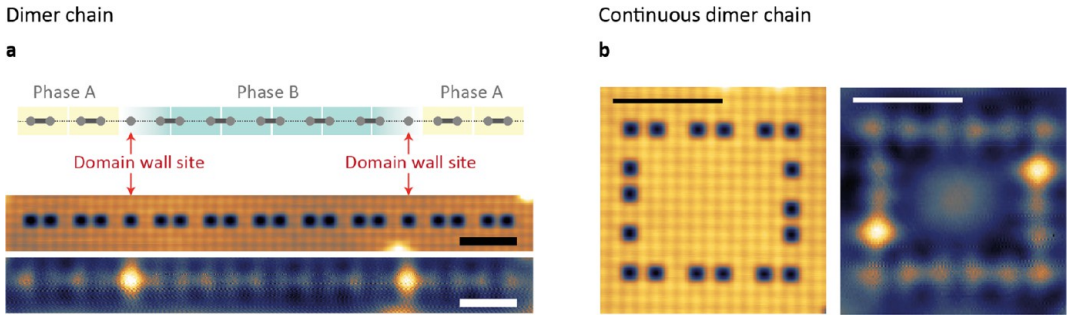


**Figure 8.** 1D SSH/dimer chain realized using vacancies in a chlorine monolayer on Cu(100). (a) Top: schematic of the configuration of the dimer chain. Heavy lines represent strong coupling, and dashed lines represent weak coupling. Two distinct phases, A and B, are denoted with yellow and blue shading. The phases are distinguished by the arrangement of bonds within and between the unit cells. Domain walls form when the phase is switched, leaving isolated sites. Middle: topographic STM scan of the chain. Bottom: differential conductance map acquired at the midgap energy (3.53 V), showing the domain wall states. Scale bars are 2 nm. (b) Left: topographic STM scan of a continuous dimer chain structure with two domain walls. Right: differential conductance map (3.5 V) showing midgap states at the domain-wall locations. Scale bars are 3 nm. Figures are adapted from ref 211. Copyright 2017 Springer Nature.

forming a Dirac cone, and the minimum (point 2) indicates the Dirac point. The two maxima correspond to the high LDOS at the M points; if the overlap integral between neighboring s orbitals is neglected, the distance between these two maxima provides a good estimate for two times the hopping term between the nearest-neighbor s orbitals, i.e., $t_{ss}$. The obtained $t_{ss}$ value is 45 meV. From a tight-binding fit, taking the overlap into account, one can find a hopping energy of 60 meV. In the lattice studied by Gomes et al. the hopping energy was about 90 meV.

Around 0 V, a very strong LDOS peak is observed on the bridge sites, while the LDOS on the lattice sites is very low (peak 4). This high electron probability corresponds to the flat band originating from p orbitals. Between 0.1 and 0.4 V, a second double peak with a minimum is found. Comparison with the calculations showed that this feature reflects the dispersive p orbital bands; the minimum corresponds to the Dirac point (point 6), and the lower maximum (peak 5) reflects the high LDOS at the M point. The maximum at higher energy (peak 7) corresponds to the third and fourth p orbital bands. If the orbital overlap and hybridization are neglected, the energy difference between the flat band maximum and the Dirac point is 1.5 $t_{pp\sigma}$; from this, $t_{pp\sigma}$ is found to be 160 meV. From the muffin-tin calculations combined with a tight-binding fit, a comparable value of 127 meV is found.

The electron probability pattern at the flat-band energy is remarkable, with a very high electron probability between the sites (thus bridge positions) and a very low probability on the sites (Figure 7d). The interaction of in-plane p orbitals at the sites of a honeycomb lattice can best be described as orbital interference by geometric frustration.[49,236] These interference patterns were also calculated by using the original tight-binding theory, and by muffin-tin calculations combined with a tight-binding parameter fit; see Figure 7e.

These results show that solid-state electronic honeycomb lattices can be designed in such a way that in-plane p orbital physics fully emerges. The design is purely based on the lattice geometry and the degree of quantum confinement and intersite coupling. These concepts can be directly transferred to two-dimensional semiconductors in which the honeycomb geometry is lithographically patterned or obtained by nanocrystal assembly;[20] see the last section of this Review. These systems can be incorporated in transistor-type devices in which the Fermi level and thus the density of the electron gas can be fully controlled.[261] For instance, a partial filling of the flat band can result in electronic Wigner crystals, new magnetic phases, and superconductivity.[49,262] Hence, Gardenier et al. present a feasible geometric platform for real materials opening the gate to novel electronic quantum phases, both in the single-particle regime as in the regime with strong interactions.[15,22,81,263]

## 8. ARTIFICIAL TOPOLOGICAL LATTICES

The versatility of artificial matter constructed one atom at a time is further demonstrated by the creation and measurement of topological states of matter. Here, we focus on experimental developments within topology that have made use of atomic manipulation platforms.

### The Su–Schrieffer–Heeger Model

**Background.** The SSH (Su–Schrieffer–Heeger) model, sometimes known as a Peierl's or dimer chain, is a one-dimensional chain of alternating weak and strong bonds. This configuration is known to occur in polyacetylene, for which the model was initially developed.[264,265] The SSH model is perhaps the simplest system that supports topological states. The dimerization of the lattice gives rise to two bulk bands, separated by a gap. Through the choice of unit cell, the state at the end of the lattice may either form part of the bulk band or an isolated end mode. This is due to either strong or weak coupling at the termination. Alternatively, one may construct a domain wall where the unit cell is switched midlattice to produce an isolated state. The crucial protecting symmetry for the isolated end or domain wall states is chiral, or sublattice symmetry. A topological state in one sublattice is robust against perturbations of the other sublattice, such as on-site energy fluctuations and the introduction of next-nearest-neighbor coupling between sites of the other sublattice. The SSH model has been implemented experimentally with a host of methods, including self-assembly of indium on Si(111),[266] with graphene nanoribbons[267,268] and in transition-metal monochalcogenide nanowires.[269] Here, we discuss the implementation of the SSH chain created "atom by atom" with scanning tunneling microscopy.

**Realization of the SSH Chain in the CuCl Monolayer on Cu(111).** As mentioned in section 6, tunable lattices can be created using a chlorine monolayer on Cu(100). Each vacancy in the chlorine monolayer hosts a well-defined state at an


https://doi.org/10.1021/acsnanoscienceau.1c00054
ACS Nanosci. Au 2022, 2, 198–224

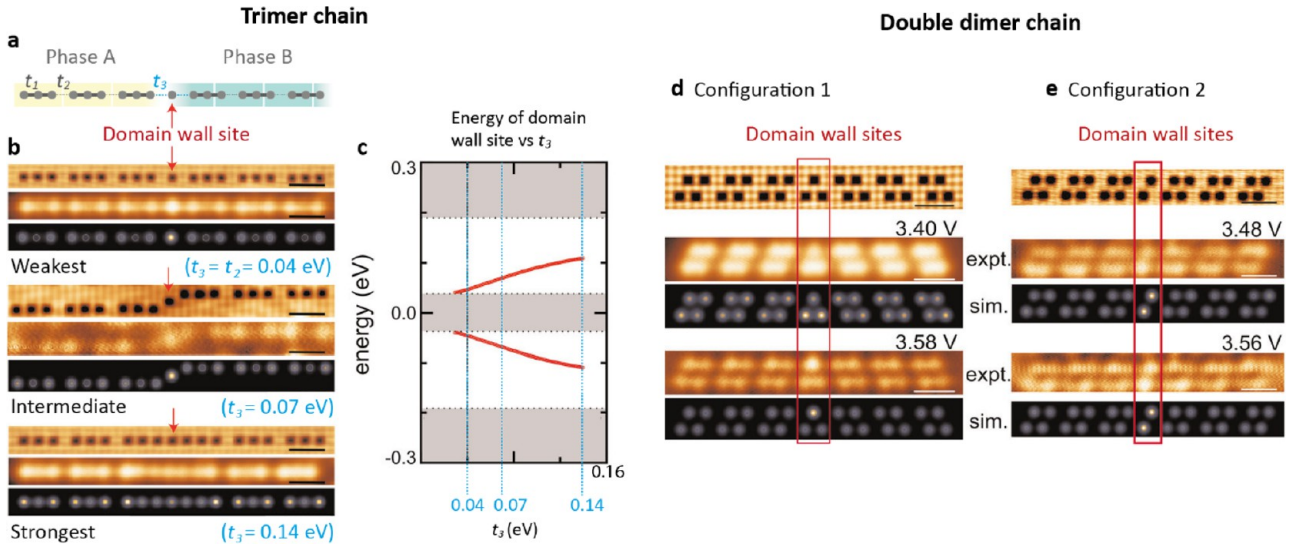


**Figure 9.** Trimer chains and double dimer chains realized using vacancies in a chlorine monolayer on Cu(100). (a) Diagram showing the arrangements of strong bonds ($t_1$, heavy lines) and weak bonds ($t_2$, dashed lines) in each type of unit cell (either yellow or blue). Between phase A and phase B, there is a domain wall site. The bonds connecting to the domain wall site are denoted $t_3$. (b) Topographical images, differential conductance maps, and simulated LDOS maps acquired at the energy of each domain wall state for three different values of $t_3$ (labeled weakest, intermediate, and strongest). (c) Tight-binding-calculated energies of the in-gap states for a trimer as a function of $t_3$. The energies are given with respect to the on-site energy of a site in the chain. The gray horizontal sections are the bulk bands. Vertical blue lines show the positions of each of the in-gap states that were realized in (b). The darker line at 0.04 eV is where $t_2 = t_3$. (d) Top: Topographs of the chains. Middle and bottom: experimental and simulated LDOS maps acquired at the energies of the domain wall states. The domain wall of configuration 1 shifts the dimerization in one chain, giving rise to three domain wall sites which are separated from the rest of the chain. Domain wall states are seen at 3.40 and 3.58 V. (e) The domain wall of configuration 2 shifts the dimerization of both chains, giving rise to two domain wall sites which are separated from the rest of the chain. Domain wall states are seen at 3.48 and 3.56 V. Reproduced from Figures 3 and 4 of ref 271, which have been reordered. The original article was published under a Creative Commons Attribution 4.0 International License.

energy below the band edge of the chlorine monolayer. The vacancies themselves can be manipulated with the STM tip and constitute artificial sites. When brought close enough to each other, the vacancies interact. In this way, the direct lattice (not the inverse as with CO/Cu(111)) can be formed. The coupling strength can be tuned by the distance between vacancies/artificial lattice sites. Drost et al. used this technique to produce several configurations of the SSH chain, which they performed d$I$/d$V$ spectroscopy measurements on to determine topological states.[211,270]

A realization of the SSH chain by Drost and co-workers is shown in Figure 8a. They produced a chain of dimers terminated by strong bonds. In this case, the interunit cell hopping is weak and hopping within the unit cell is strong, giving rise to two sets of states above and below the vacancy state energy. At two points in the chain, domain walls were introduced (see schematic (top) and STM scan (center) in Figure 8a), manifesting sites solely connected by weak hopping. d$I$/d$V$ spectroscopy revealed in-gap states localized at the isolated sites created by the domain walls. A differential conductance map of the chain at this in-gap energy shows a pronounced intensity at the domain wall sites, corresponding to the topologically protected domain wall states of the SSH model (bottom part of Figure 8a).

To verify that the form of the chain had no effect on the existence of the midgap states, the authors constructed a loop of artificial sites with SSH texture and embedded two weakly connected domain wall sites within it. An STM scan of the loop is shown in Figure 8b (left). In this configuration, in-gap states were also identified at the isolated sites formed by domain walls, which are prominently visible in the differential conductance map in Figure 8b (right).

**Trimer Chains.** In subsequent research from the same group, Huda et al. expanded the work on topological domain wall states by creating a chain of trimers with various domain configurations.[271] The design of the trimer chain considered is shown in Figure 9a. Each unit cell contains three sites. To define two different phases (labeled A and B) in the chain, the bond configuration within each cell is chosen differently. For the combination chosen here, localized states emerge at the domain wall between phases A and B. The states lie within the gaps in the band structure, which itself contains three energy bands. It was shown that the energy level positions could be tuned by altering the coupling between bulk and domain wall sites (hopping $t_3$ in Figure 9). This is in contrast to that of a dimer chain (the SSH model described above), where the energy of the domain wall state is pinned exactly in the middle of the gap for symmetry reasons. Figure 9c shows the variation of the domain wall site energy as $t_3$ is altered. The three gray bars are the bulk bands which remain unchanged. Meanwhile, the two energy states of the domain wall site both deviate toward the middle of their respective gaps as $t_3$ is increased. The group altered $t_3$ in their trimer lattice by changing the physical distance between sites at the domain wall. $t_3$ was weakest when it was equal to the weak coupling of the rest of the lattice. From there, the physical gap between sites at the domain wall was made successively smaller for stronger coupling. Figure 9b shows an STM topograph, differential conductance map, and LDOS calculated with tight binding for each lattice. The LDOS maps, both experimental and calculated, have been produced at the energies of the domain wall sites. This result showed that topological states could be produced in trimer chains, with the extra feature that the energy levels of the topological modes could be tuned at will


https://doi.org/10.1021/acsnanoscienceau.1c00054
ACS Nanosci. Au 2022, 2, 198−224

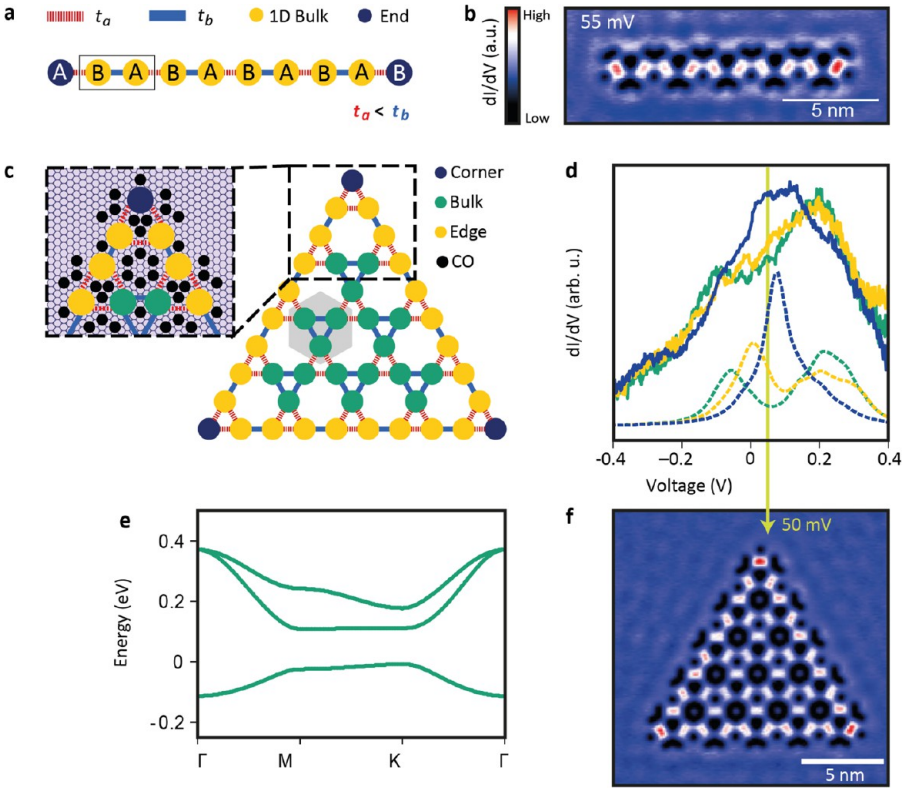


**Figure 10.** From 1D SSH to 2D breathing Kagome lattice. (a) Schematic of the SSH model with sublattices A and B and alternating weak (red) and strong (blue) coupling. (b) Differential conductance map of the realized SSH chain at V = 55 mV showing localized modes at the end sites. (c) Schematic of the breathing Kagome lattice and the design for its realization using CO on Cu(111) (inset). (d) Differential conductance spectra acquired in the bulk (green) at the edges (yellow) and at the corners (blue) of the Kagome lattice. The solid lines are from experimental data, and the dashed lines are from tight binding calculations. (e) Band structure of the breathing Kagome lattice showing a band gap between the two lowest bands. In the displayed realization, there is a next-nearest-neighbor hopping of 18.8 meV, resulting in a nonflat top band ($t_a$ = 28.5 meV, $t_b$ = 75 meV). (f) Differential-conductance map of the realized breathing Kagome lattice at V = 50 mV showing localized modes at the corner sites. Figures are adapted with permission from ref 272. Copyright 2019 Springer Nature.

using the Cl/Cu(100) platform. Such states are thought to house fractional charge of $e/3$ or $2e/3$ depending on the domain wall configuration.

**Double Dimer Chains.** Huda et al. also investigated double dimer chains. Here, the sublattice symmetry is broken due to coupling between the two chains, however, domain wall states arise from another topological origin.[266] The states can host different chirality depending on the configuration of the chains and domain wall. Figure 9d and e show two examples of double dimer lattices produced with the Cl/Cu(100) platform. In Figure 9d, the dimerization has been shifted in only the top chain, which produces three domain wall sites. These contribute three states, one of which merges into the bulk. Differential conductance maps were acquired at the remaining two energies, shown in Figure 9d. In Figure 9e, the dimerization has been shifted in both lattices, which results in two domain wall sites. This configuration also produced three energy states; the bonding and antibonding states of the isolated dimer, as well as a hybridization of the domain wall with the middle bulk band. By performing these experiments, the group showed that chirality is a degree of freedom that can be manipulated with artificial lattices.

**SSH Chain Simulated with CO on Cu(111).** Similar to the chlorine vacancy platform, the SSH chain can be realized using the CO/Cu(111) platform.[272] An example of a finite SSH chain is shown in Figure 10a. The yellow sites indicate bulk artificial-atom sites connected by alternating weak (red, dashed) and strong (blue, solid) bonds. The end sites, indicated in blue, are weakly connected to the bulk. The weak and strong bonds are engineered by narrow and wide connections between the sites, respectively, defined by the positions of the CO molecules. A differential-conductance map around midgap energy, 55 mV, confirms a pronounced LDOS at the end sites (see Figure 10b), corresponding to the topological end states in the SSH model. Some intensity is observed in the bulk as well, which can be ascribed to the finite weak coupling ($t_a$ = 28.5 meV and $t_b$ = 75 meV; parameters were derived from a comparison between a muffin-tin and tight-binding model for the described lattice configuration).

## Corner States in a Breathing Kagome Lattice

The concept of localized modes on weakly connected sites can be generalized from 1D to 2D. Kempkes et al.[272] realized a finite breathing Kagome lattice using the CO/Cu(111) platform. A compelling artificial Kagome lattice could also be created by an organic molecular synthesis on the surface of Cu(111).[95] A conventional Kagome lattice is a tripartite lattice that can be considered as a line graph of the honeycomb lattice.[218] This lattice can exhibit a topological flat band and a Dirac cone in the presence of spin−orbit coupling.[218] The *breathing* Kagome lattice[273] has alternating weak (red, dashed) and strong (blue, solid) hopping, opening a band gap between the bottom Dirac bands; see Figure 10c−e. Importantly, the corners (dark blue) only have weak bonds to the rest of the


https://doi.org/10.1021/acsnanoscienceau.1c00054
ACS Nanosci. Au 2022, 2, 198−224

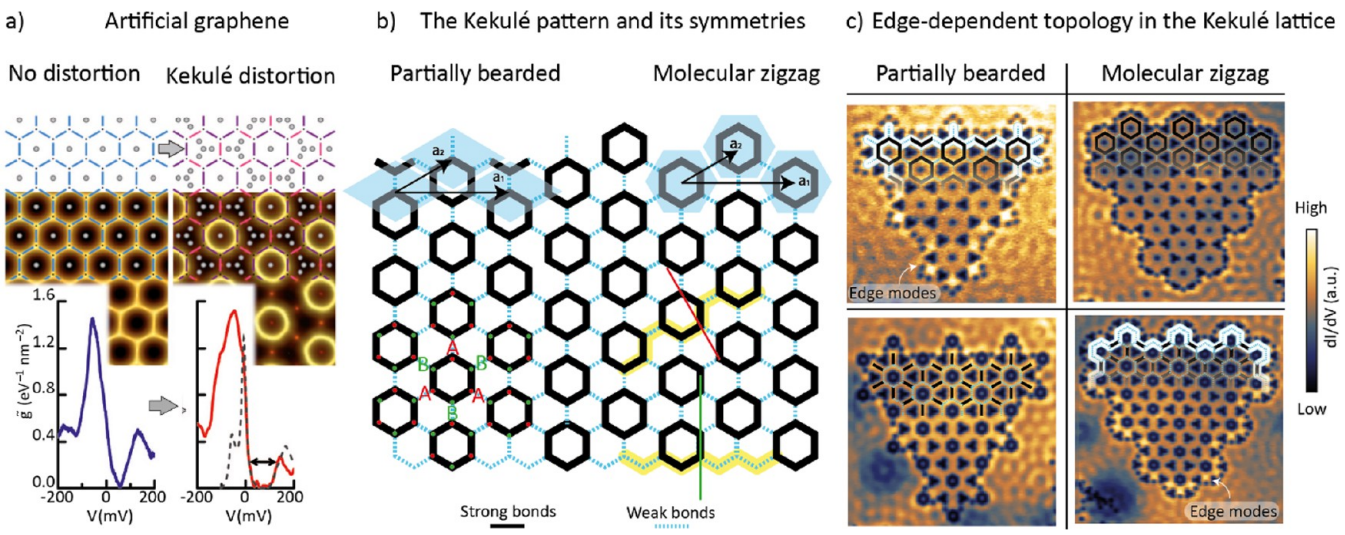


**Figure 11.** Topology in Kekulé lattices (a) The first realization of a honeycomb lattice with Kekulé texture, produced with the CO/Cu(111) platform. On the left is a plain artificial graphene lattice, with the bond structure (top) and STM image (center) shown. Black dots represent artificial electronic sites, gray dots represent CO molecules, and blue lines represent a uniform bond strength. The d$I$/d$V$ spectrum on the bottom left was acquired in the artificial graphene lattice and shows evidence of the Dirac point at around 50 mV. The right side of the image illustrates a Kekulé lattice, which is a honeycomb lattice with modulated bonds, where purple represents strong and pink represents weak coupling. The d$I$/d$V$ spectrum on the bottom right was acquired in the Kekulé lattice and exhibits a gap compared to the plain honeycomb lattice. This a result of the Kekulé modulation. (b) Illustration of the protective symmetries and example terminations in the Kekulé lattice. Unit cells are defined in blue for two edges: partially bearded and molecular zigzag. For the existence of topological states, sublattice symmetry and mirror symmetry must be present. The two sublattices are denoted by A (red dots) and B (green dots). Two mirror planes are shown, one perpendicular to the $a_1$ lattice vector (red) and one perpendicular to $a_2$ (green). There is no lattice site to place the plane that would yield mirror symmetry perpendicular to $a_2$, but it can be done for $a_1$. (c) Experimental realizations of the Kekulé lattice with different terminations and bond patterns. The two top lattices have intra-hexagon bonds stronger than inter-hexagon bonds. The opposite holds for the lower two lattices. The lattices on the left have partially bearded termination, and on the right, molecular zigzag. The top left and bottom right lattices exhibit edge states, as highlighted.[288]. Figure 11a reprinted by permission from ref 215. Copyright 2012 Springer Nature. Figure 11c adapted with permission from ref 288. Copyright 2020 the American Physical Society.

lattice. Furthermore, the lattice consists of dimerized boundaries (yellow), reminiscent of SSH chains, and a trimerized bulk (green). An enhanced LDOS results on the corner sites in both the band gap of the SSH-like edges and the band gap of the bulk (green) (spectra not shown). The LDOS at this energy is spatially visualized in the differential conductance map in Figure 10f. This confirms that localized in-gap modes are present on weakly coupled sites in the presence of the 2D lattice. Additionally, localized in-gap modes could be added or removed at will, showing the tunability of the platform.

While the topological end-modes of the 1D SSH chain and the corner modes of the 2D breathing Kagome lattice emerge in a similar way in the wave function maps, it does not inherently follow that the latter are protected as well. Initially, it was suggested that the breathing Kagome lattice is a higher-order topological insulator (HOTI).[274,275] The "order" refers to the difference $n$ in dimensionality between the $d$-dimensional bulk and the $(d-n)$ topologically protected states, presumably making the Kagome lattice with $d = 2$ and $n = 0$ a second order TI. The 0D corner modes and 1D hinge modes in 2D and 3D second order TIs, respectively, are topologically protected by spatial symmetries or time-reversal symmetry, or a combination of both.[274−277] Soon after the theoretical concept had been introduced, several existing materials were shown to be HOTIs.[277,278] In addition, HOTIs were created using platforms with different types of excitation, such as photonic lattices,[279] mechanical metamaterials,[280] microwave circuits,[281] and topolectrical circuits.[282] A 3D electronic HOTI exists as a real material, e.g., the metal bismuth.[278] 2D electronic HOTIs were predicted for several metal dichalcogenides,[277] but experimental realizations had not been reported so far. Several protection mechanisms were proposed for the corner modes in the Kagome lattice, among which a combination of mirror and $C_3$ symmetry[273] and a generalized chiral symmetry.[272,283,284] Recently, however, it was shown by van Miert and Ortix that this does not hold.[285] The nature and robustness of the corner-localized modes in the breathing Kagome lattice are under debate.[285,286]

## The Kekulé Lattice

Another sort of lattice that can host topological states is the Kekulé lattice. This is a honeycomb lattice, like graphene, but with alternating weak and strong bonds. The band structure of a plain honeycomb lattice consists of Dirac cones at the K and K' points, describing massless electrons. When the bonds in a honeycomb lattice are modulated with the Kekulé distortion, a gap opens at the K points, which is equivalent to ascribing a mass to the electron in the Dirac equation. In this case, the bulk of the Kekulé lattice becomes insulating, i.e., a gap is opened in the band structure. The remarkable feature of the Kekulé lattice is that, within this gap, topologically protected edge states can exist, but only for certain configurations of the lattice and its termination. This type of topology occurs in *topological crystalline insulators*. These are states of topological matter that cannot be adiabatically transformed into trivial insulators unless a certain spatial symmetry is broken, such as mirror or rotational symmetry.[287] In the case of the Kekulé lattice, mirror and sublattice symmetries are the protective symmetries of interest.


https://doi.org/10.1021/acsnanoscienceau.1c00054
ACS Nanosci. Au 2022, 2, 198−224

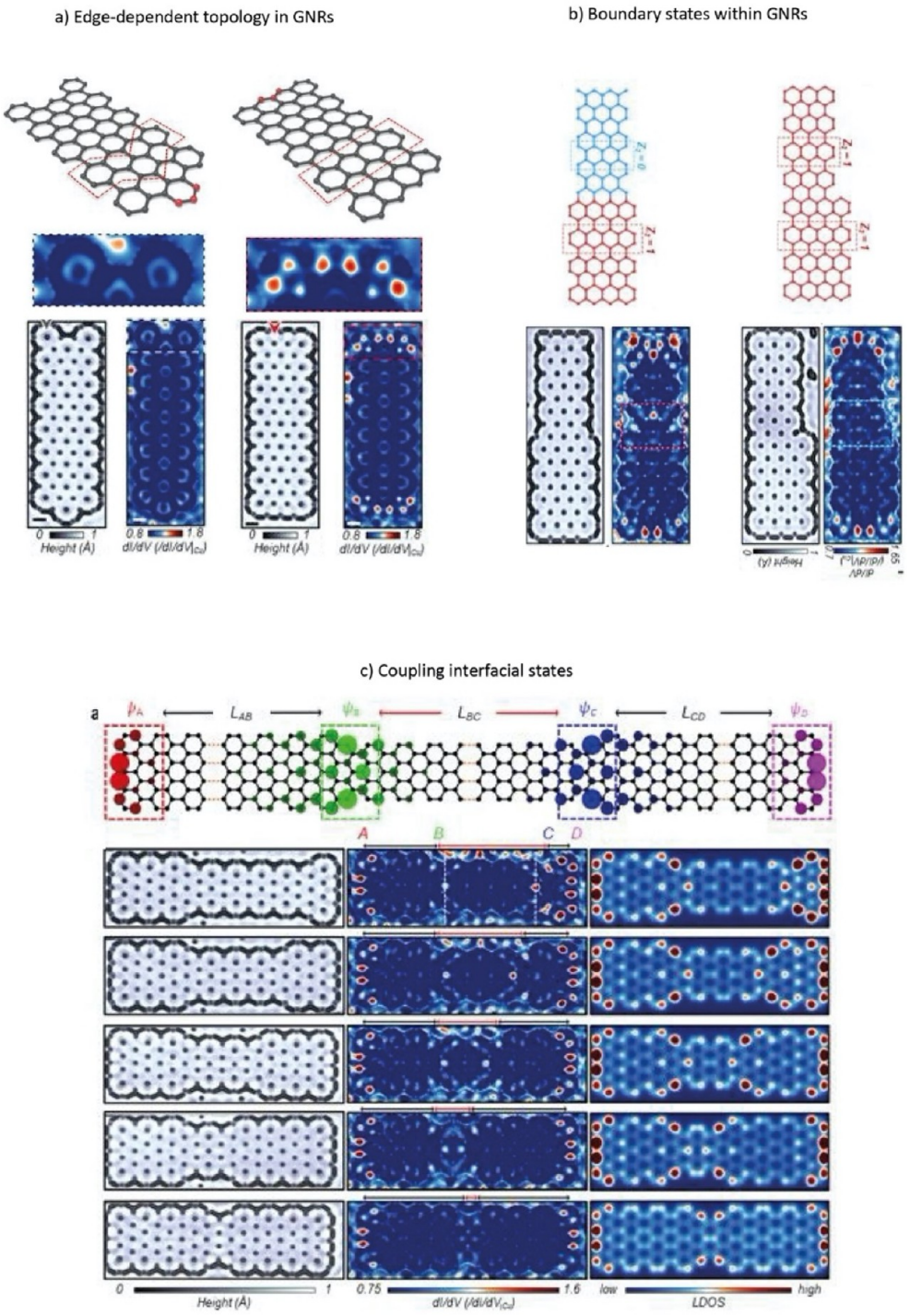


**Figure 12.** Topological states in artificial graphene nanoribbons. (a) Top: Two different GNR designs, the left has a molecular zigzag edge and the right has a zigzag edge. STM topographs are shown in a black/white color scheme. d$I$/d$V$ maps are shown in a blue/white/red color scale and show that the molecular zigzag GNR is trivial and the zigzag GNR accommodates edge modes. (b) Symmetrical (left) and asymmetrical (right) 7−9 GNRs. The STM topographs show the geometry in a black/white color scheme. The d$I$/d$V$ maps show that there is a state at the interface in the symmetrical case but not the asymmetrical case. (c) Top: Schematic of the GNR. Bottom: STM topographs, d$I$/d$V$ maps, and tight-binding calculated LDOS maps are shown for several configurations where the lengths of each section are varied progressively. The edge modes are seen to couple with each other, as evidenced by the diminishing LDOS of the interfacial states, indicating hybridization of the states at both ends. Figures are taken from the following preprint: ref 344.

Although the Kekulé distortion in the honeycomb lattice has not been reported to exist in nature, Kekulé lattices have been artificially produced in experiments. The first realization of the Kekulé lattice was produced by Manoharan et al. by confining the Cu(111) surface state with CO.[215] There was a clear energy gap at the Dirac point, measured in the d$I$/d$V$ spectrum. Figure 11a shows (from top to bottom) the design, an STM image, and a d$I$/d$V$ spectrum, respectively, for artificial graphene. The right side of Figure 11a shows the same for a lattice with a Kekulé distortion. The d$I$/d$V$ spectrum


https://doi.org/10.1021/acsnanoscienceau.1c00054
ACS Nanosci. Au 2022, 2, 198−224

shows a gap compared to the undistorted graphene. From fits to theory, they found the mass of the Fermions in this Kekulé system to be $0.1 \pm 0.02 m_e$ (as opposed to zero in theory for Fermions in graphene).

Later, topological modes were identified in a photonic structure, where zero modes were localized at the corner of a 2D Kekulé system.[279] Edge states have also been observed in a sonic Kekulé lattice.[289] It was previously thought that topological states in the Kekulé lattice came about via a quantum pseudospin Hall effect accommodated by orbital angular momentum at the hexagons. This was postulated by Hu and Hu, who at that time implied that merely switching the configuration of strong and weak bonds could lead to the existence or absence of topological states.[290] Later, the same group found that this was not entirely true: the shape of the edge should also be taken into account.[291] The existence of topological states at the edge of the Kekulé lattice was predicted by the group by calculating the mirror winding number, which acts as the topological invariant of the system. The protective symmetries of the Kekulé lattice in this model are mirror symmetry and sublattice (chiral) symmetry. The sublattice symmetry of the system is captured by the two overlapping triangular lattices, where each A (B) site is connected only to B (A) sites, illustrated in Figure 11b. Mirror symmetry is also elucidated in Figure 11b. There is mirror symmetry about the plane perpendicular to $\mathbf{a}_1$ (zigzag direction) but not about the plane perpendicular to $\mathbf{a}_2$ (armchair direction), where there is no site at which the geometry can be mirrored at an axis perpendicular to the edge. Thus, no mirror winding number can be calculated for the graphene armchair edge. The mirror symmetry allows the decomposition of the Hamiltonian into even and odd sectors, which can ultimately be used to find two mirror winding numbers. In order to have a correspondence between the edge modes and the winding number, the unit cell must be chosen in such a way that it is not severed at the edges. Thus, the mirror winding numbers depend on the sublattice and mirror symmetries, and the unit cell. By extension, the bond texture of the lattice and the shape of the edges are both crucial to the topology of the system. When the sum of the winding numbers is zero, this results in a dispersive edge state. In the case of the zigzag edge, the mirror winding numbers can be calculated, and they are nonzero, thus the states are static. However, one can conceive of edges where the total mirror winding number is zero. Two examples presented here are the partially bearded and molecular zigzag edges. Figure 11b shows the bond pattern and unit cells defining these edges.

The Kekulé lattices with partially bearded and molecular zigzag terminations were realized using the CO/Cu(111) platform in the STM.[288] The bonds between lattice sites were made stronger or weaker through the strategic placement of CO molecules. Figure 11c presents differential conductance maps taken in the bulk band gap of each lattice. Elevated LDOS($E$,$x$,$y$) at the edges can be observed in the maps on the top left and bottom right of Figure 11c, while the lattices shown at the top right and bottom left are insulating throughout. This set of experiments provided an experimental validation of the theoretical paper by Hu et al. (ref 289), who predicted the existence of the edge states shown.

## Toward Majorana Bound States in Artificial Lattices

There is a very active research effort devoted to realizing Majorana bound states (MBS) in condensed matter systems. These exotic quasi-particles, the physics of which will not be expanded upon here, can be used in fault-tolerant quantum computing. One of the avenues being explored to fabricate MBs is based on one-dimensional magnetic chains on conventional superconductors. In these systems, the MBS should emerge at the chain ends. Indeed, signatures consistent with Majorana modes—an enhanced density of states at zero energy - have been observed in self-assembled Fe chains on Pb(110).[292,293] In principle, superconducting or magnetic tips can be used to distinguish Majorana modes from other phenomena that might also lead to zero energy states. Thus, far, controlled manipulation of adsorbates on Pb surfaces has not been reported. This limits the possible network architectures that can be used to study Majorana physics. Consequently, different research groups have worked on creating chains of metal atoms with noncolinear spin-structure on superconductors that allow for atomic scale manipulation. Atomically well-defined Fe chains could be constructed on Re(0001) and Nb(110), and zero bias states were observed for sufficiently long chains.[294−296] In these systems, the (magnetic) coupling between the atoms depends on the crystallographic direction in which the chain is build. This was also exploited to engineer MBS in Mn chains on superconducting Nb(110) [arXiv:2104.11503]. The atomic scale control allows for the manipulation of interactions between Majorana modes in finite size systems, which is an essential ingredient for Majorana-based quantum computing.

## Artificial Graphene Nanoribbons

Changing the nature of topological boundaries in a material was also achieved in artificial graphene nanoribbons [arXiv:2104.11334] (GNRs). In this work, the authors constructed strips of artificial graphene using the CO/Cu(111) platform. GNRs have been known to host topological modes at their edges.[68,297] Here, the authors engineered this behavior and showed that the topological states were tunable.

First, 9-atom wide armchair GNRs were constructed. Topological states were engineered at the ends of the ribbon by editing the geometry: when the ends were made to have a zigzag pattern, topological edge states arose. When three sites were moved from one zigzag edge to the other, creating instead a “molecular zigzag” type pattern at both sides, the topological states became trivial. This was made clear with d$I$/d$V$ spectroscopy and maps, as presented in Figure 12a.

To verify that this effect had not been misconstrued as edge states from other mechanisms, the group connected 7-wide and 9-wide artificial GNRs together in two different ways, either symmetric or asymmetric. In the symmetric case, a topological interface state appears, while in the asymmetric case it does not. This is because the unit cell depends on the termination of the 7-wide GNR, which in turn depends on whether it is connected directly at the center (symmetric) or to one side (asymmetric) of the 9-wide GNR. This is shown in Figure 12b. Finally, the group investigated coupling between interfacial states by constructing a 9GNR/7GNR/9GNR structure containing four topological states. Shifting one of the domain walls closer to another step-by-step showed that the LDOS of the topological states diminished with decreasing distance (increasing coupling strength) between them. The group conjectured that this was a result of the hybridizaion of the wave functions at both ends. This can be seen in Figure 12c.


https://doi.org/10.1021/acsnanoscienceau.1c00054
ACS Nanosci. Au 2022, 2, 198−224

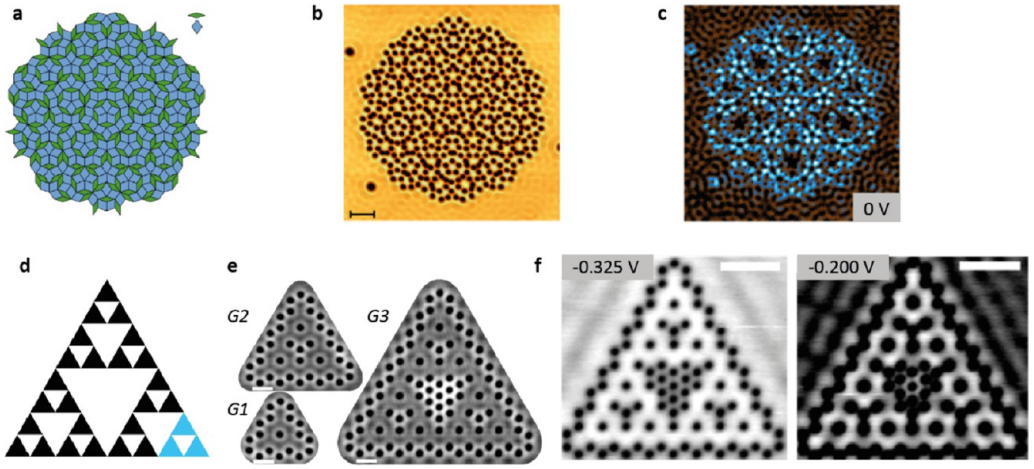


**Figure 13.** Aperiodic lattices created using the CO/Cu(111) platform. (a) Penrose tiling, constructed with two rhombi, indicated in blue and green. (b) STM image (left) of an arrangement of CO molecules (black) that leads to a Penrose tiling for the surface- state electrons. (c) The corresponding normalized d$I$/d$V$ map (right) shows that the LDOS also exhibits a Penrose geometry. Scale bar: 5 nm. (d) Third generation Sierpinksi triangle. The first generation is shown in light blue. (e) STM images of the first three generations of the Sierpinski triangle, indicated by G1, G2, and G3, respectively. Scale bar: 2 nm. (f) Left: dI/dV (LDOS) map of the electronic state at −0.325 V; the absence of nodal points indicates a fully bonding wave function delocalized over the triangle. Right: d$I$/d$V$ (LDOS) map of the electronic state at −0.200 V; nodal points partition the wave function into nine self-replicating parts. Panels b and c are taken from ref 309, published under a Creative Commons Attribution 4.0 International License. Panels e and f are adapted with permission from ref 317. Copyright 2019 Springer Nature.

## 9. SIMULATION OF APERIODIC TWO-DIMENSIONAL SYSTEMS

### General

The presence of long-range order and translational symmetry enables the use of periodic boundary conditions in electronic structure calculations. As such, it underpins our understanding of the electronic structure of materials. However, not all materials have translational symmetry. There are three notable categories: (i) *Amorphous materials*, i.e., materials with no long-range order. In amorphous systems, the atomic regularity seems to be present if examined from afar. In reality, the atoms have positions that are centered around a mean value (those of the corresponding crystal), but the coordinates differ randomly from site to site. This nonperiodicity results in localization of wave functions and a "band structure" that bears some reminiscence to that of the crystalline variant. A well-known example is amorphous silicon; it has "quasi" conduction and valence bands with broad tails, and optical transitions from the quasi-VB to quasi-CB set on at around 1.6 eV instead of 1.1 eV in crystalline Si. (ii) *Quasicrystals, aperiodic tilings*, built up using two or more well-defined tiles. In so-called quasi-crystals, motifs (tiles) are tessellated such that there is local rotational symmetry but no translational symmetry. Quasi-crystals are rarely found in nature; Schechtman et al.[298] observed metallic alloys in which the atoms are arranged in motifs with 10-fold rotational order, being incompatible with a periodic lattice. Later, quasi-crystalline motifs have been observed in some types of self-assembled colloidal solids.[299,300] (iii) *Fractals*, systems that are self-similar on different length scales. For fractals, the so-called Hausdorff dimension is a noninteger that exceeds its topological dimension. Regular fractals consist of motifs that are repeated on several length scales; fractals often emerge in bioinorganic skeletons and plants, for instance, in the Romanesco flower. Fractal structures have been obtained with synthetic chemistry.[301,302]

Figure 13 shows an example of a quasi-crystal (Penrose tiling) and fractal (Sierpinski triangle). The electronic properties of both types of structure are difficult to study, since they rarely occur in nature on an appropriately small length scale. Periodic Bloch-type wave functions do not occur in solids that lack atomic order. Many quasi-crystals, experimentally discovered in the early 1980s,[303,304] have to be synthesized in the laboratory and are thermodynamically unstable. The few quasi-crystals that have been found in nature have been formed in outer space.[305] Even though fractals are pervasive on the macroscopic scale (Romanesco broccoli, the cardiovascular system, and coast lines are well-known examples), no naturally occurring geometric quantum fractals have been identified. Molecular self-assembly can be used to form fractals in a bottom-up fashion.[301] However, the coupling between the building blocks is too weak to result in a true electronic fractal. The ability to position adsorbates with atomic scale precision enables the formation of well-defined electronic quasi-crystals and fractals, as shown below. Synthetic quasi-crystals have also been realized using cold atom gases and photonics.[306−308]

### Formation of Electronic Quasicrystals and Fractals

Collins et al. used the CO/Cu(111) platform to create an electronic Penrose tiling; see Figure 13a−c.[309] The motifs in the Penrose structure contain several specific sites, each with its own vertex structure. It was shown that these different sites are characterized by a specific local density of states, LDOS(E). In energy-resolved wave function maps, these sites have heightened LDOS in the Penrose tiling at specific energies.

Fractal structures in which electrons are confined remain intriguing to the scientific community.[310−316] The same technique used for the creation of electronic lattices and simulations of quasi-crystals has been used to create simulations of electronic fractals, for instance a Sierpinski triangle; see Figure 13d−f.[317] The basic unit, generation 1 (G1), contains three different types of atomic sites, characterized by their connectivity or vertex structure. The wave function maps in the second and third generation of the Sierpinski gasket show remarkable regularities, which can


https://doi.org/10.1021/acsnanoscienceau.1c00054
ACS Nanosci. Au 2022, 2, 198−224

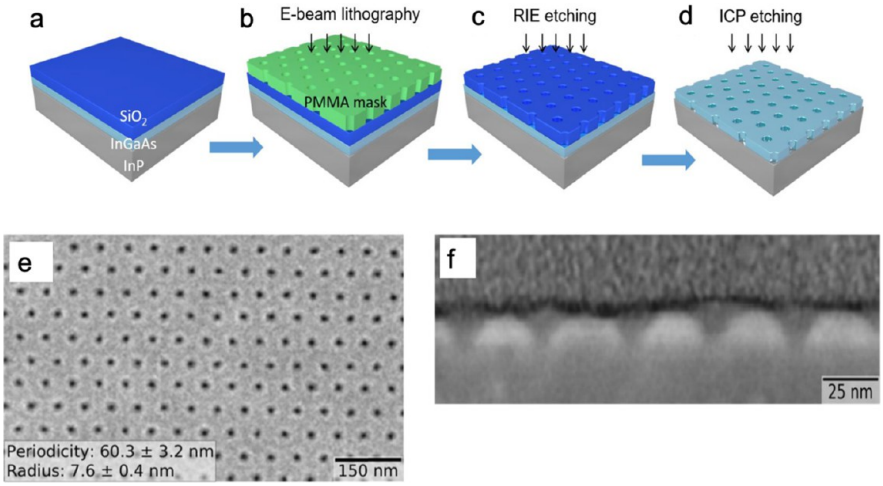


**Figure 14.** Fabrication of 2D InGaAs semiconductor with a nanoscale honeycomb geometry. (a–d) Consecutive steps in the nanolithography procedure, with (a) growth of silica and PMMA layers on top of the InGaAS quantum well, after which (b) electron beam lithography is used to write a hexagonal periodic pattern in the PMMA; (c) presents the reactive ion etching to transfer the pattern as hole array in the silica layer, and (d) presents the inductive coupled plasma etching to transfer the hole pattern from the silica into the InGaAs layer. (e) SEM image of a honeycomb InGaAS crystal with a periodicity of 60 nm. (f) SEM cross section of the conical holes with periodicity of 39 nm. Reprinted from ref 262. Copyright 2021 American Chemical Society.

loosely be understood by molecular orbital theory. The resonance at lowest energy shows a wave function which is entirely "bonding", i.e., has the same sign everywhere, visible by a nearly uniform LDOS over the entire fractal structure without nodes in the squared wave function $|\varphi|^2(E)$ . At higher energy, nodal points emerge in the wave function as for molecules. Interestingly, these nodal points partition the wave function in self-repeating parts; see Figure 13f. Hence, the electronic wave functions inherit the structure (and fractal dimensions) of the underlying "atomic" structure. This is consistent with the observation for the synthetic Penrose tiling that the Cu(111) surface state electrons are confined to the geometric structure defined by the CO molecules. The Hausdorff dimension of a geometrical Sierpinksi triangle is log 3/log 2 ≈ 1.58. In the work, presented here, the box counting method was employed to experimentally determine the Hausdorff dimension from wave function maps of the CO/Cu(111) Sierpinski triangle at different energies. It was found to fluctuate around 1.58, confirming the fractal nature of the "lattice".

Many-body interactions between electrons affect the electronic properties of materials differently in one and two dimensions; it would thus be of high interest to be able to study electron correlations in fractal structures, such as the Sierpinski fractal in Figure 13, with a dimension between one and two. Other outstanding questions are related to the effect of spin–orbit interaction or Cooper fair formation in electronic fractals.[318,319] Quantum simulations will require electron gases with low and varying electron density to study interactions; electron gases that inherit spin–orbit coupling, or the propensity for pairing by proximity[318,319] to study the metal/superconducting transition in a fractal.

## 10. BACK TO REAL MATERIALS: GEOMETRICALLY PATTERNED TWO-DIMENSIONAL SEMICONDUCTORS

### Brief History

In semiconductors, the chemical potential of free conduction band electrons (valence band holes) can be varied with respect to the energy levels in the system. This is possible either by incorporating specific nonisovalent impurity atoms on specific atomic positions in the lattice, or by applying an external electric field, thus electrostatic doping or gating. The latter requires a capacitor structure between the semiconductor of interest and a metal electrode. In a more advanced technological form, electrostatic gating is used in complementary metal-oxide-semiconductor (CMOS) technology to define and transmit (0,1) bit states in transistor devices. More recently, also electrolyte gating has been applied.[261,320,321] The ability to grow ultrapure Si crystals, foresee them with electron-donating or electron-accepting dopants, and change the chemical potential has enabled our current information society, known as the "silicon age". In the temperature range considered here, the chemical potential is very close to the Fermi level. The ability to be able to change the Fermi-level has key scientific importance. First, being able to change the electron concentration in the conduction band (hole concentration in the valence band) allowed in-depth study of a plethora of opto-electrical and magneto-optical phenomena in which interaction of electrons, excitons and phonons play a role. Second, the energetic variation of the Fermi-level allows to scan the Fermi-level across large parts of the Brillouin zone, this enables one to study the properties of electrons at specific points in the Brillouin zone.

In parallel with the development of CMOS technology based on a bulk Si, low-dimensional and especially 2D semiconductors were developed and investigated. The electrons in 2D semiconductors correspond to Bloch type waves in the two lateral *x,y* directions and are confined as standing waves in the short *z* direction. Two-dimensional semiconductor crystals, also known as quantum wells, can be


https://doi.org/10.1021/acsnanoscienceau.1c00054
ACS Nanosci. Au 2022, 2, 198–224

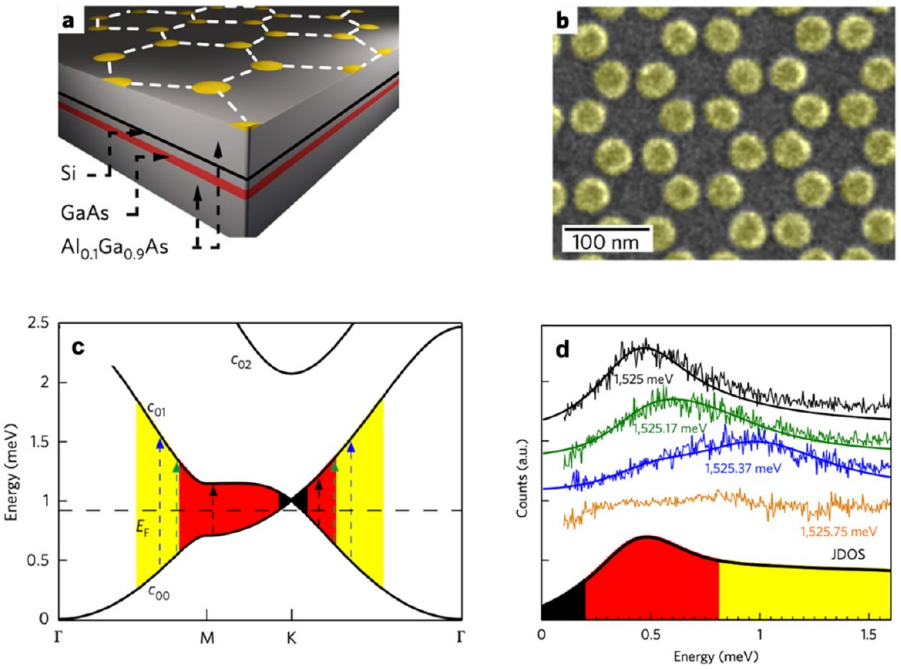


**Figure 15.** Resonant inelastic light scattering spectroscopy (RILS) of two-dimensional electron gas in GaAs confined to a honeycomb geometry. (a) Sketch of the AlGaAs/Si/GaAs heterostructure with attractive metal gates on top to force the electron gas in a honeycomb geometry. (b) SEM picture with the array of gate electrodes on top of the device. (c) Sketch of the lowest two conduction bands forming a Dirac cone, and possible intracone transitions in the 1 meV range. (d) RILS spectra (enhanced by optical pumping) showing a strong transition around the M points (0.5 meV) in the Brillouin zone. The joint density of states is indicated at the bottom. Reprinted with permission from ref 18. Copyright 2018 Springer Nature.

grown on substrates and incorporated in devices by precious gas-phase deposition techniques such as chemical vapor deposition, molecular beam epitaxy, pulsed layer deposition, and methods derived from these.[322,323] Two-dimensional semiconductors have boosted the optoelectronic industry. In addition, fundamental research on electron gases in 2D semiconductors have resulted in paradigm-shifting breakthroughs in solid state physics. In 1980, the quantum Hall phenomenon was discovered,[3,324−326] now established as the first topological electronic band structure effect in the solid state. Around 1984, the fractional quantum spin Hall effect was discovered and analyzed.[4,327−329] Further theoretical and experimental research revealed the existence of composite electronic quasi-particles, some of them with exchange statistics not reminiscent of Fermions, nor bosons, called non-Abelian anions.

Another step in this field, more related to the contents of this Review, was to modulate the lateral potential experienced by the electrons in a 2D semiconductor in a periodic way. The patterning creates a potential on the 100 nm scale superimposed on the atomic potential of the lattice. This superimposed potential results in the formation of electronic minibands and thus provides a powerful pathway to alter the electronic band structure of well-known semiconductor materials by geometry. Technically, this is achieved by electron beam lithography methods with the purpose to fabricate a periodic array of metal gates that exert a repulsive of attractive potential, forcing the electrons to live in a honeycomb superlattice. The magnitude of the translation vectors is between 150 and 100 nm.[14,250] Alternatively, an array of nanoscale holes in a 2D semiconductor crystal can be fabricated,[247,249] in fact resulting in a more robust honeycomb potential, also allowing for smaller lattice vectors. This latter method and the resulting 2D semiconductor with a honeycomb geometry with translation vector magnitudes of 40−60 nm are presented in Figure 14. A much later development came from the field of colloidal nanoscience: self-assembly and oriented attachment of PbSe nanocrystals resulted in 2D semiconductors with square or hexagonal arrays of nanovoids; the latter system is, in fact, an atomically coherent semiconductor with a honeycomb geometry.[255,256] The advantage of nanocrystal assembly is the much smaller period in the range of 5−10 nm, resulting in broader, i.e., more dispersive, electronic bands.[20,262] But obviously, nanolithography for periodic superlattices in semiconductors is better established and applicable to more type of materials.[250]

## Theoretical Efforts before the Rise of Graphene

The two-dimensional honeycomb lattice has been inspirational for many scientists, even far before the rise of graphene. As far as known, the first calculations of the band structure of an electronic honeycomb lattice were reported in 1947.[330] The theoretical efforts at the end of the previous century were devoted to honeycomb systems featuring Coulomb or spin interactions between the electrons. The on-site and nearest neighbor Coulomb interactions, and the resulting semimetal/insulator model were discussed in terms of the Hubbard model.[331−335] Coulomb interactions and magnetic ordering were discussed in detail by Herbut et al. showing that the on-site Coulomb interactions drive a semimetal to antiferromagnetic insulating phase transition.[335]

The single-electron band structure of two-dimensional semiconductors with a honeycomb geometry got the interest of theorists at the end of the previous century up to this date.[14,20,249,253,336−338] The low-energy band structure shows several Dirac cone mini-bands, similar as those predicted and


https://doi.org/10.1021/acsnanoscienceau.1c00054
ACS Nanosci. Au 2022, 2, 198−224

measured for the artificial honeycomb lattices formed on a Cu(111) surface; see section 7. However, the orbital nature of the bands and the interesting physics of in-plane p orbitals, where destructive orbital interference results in a flat band, were not discussed in the early works. The physics of in-plane p orbitals was first mentioned by the group of Das Sarma[49,236] and related to experimental research with cold atoms in optical lattices. Dirac cones and flat bands arising from the interaction of on-site s, p, ... orbitals were explicitly discussed in 2014, using atomistic calculations.[20] It is interesting to see that, provided that hybridization between the s and p orbitals is absent, the band structure of a honeycomb lattice is generic and holds for artificial lattices and semiconductors. The band structure has been predicted by theory on several levels, from simple tight-binding approaches[260] to the muffin-tin approximation[247,262] to atomistic theories for semiconductor.[339] This generic band structure in the low-energy region consists of two s-bands that form a Dirac cone, followed by for p-bands, i.e., a Dirac cone between two flat bands (see Figure 7)

### Magneto-optical and Magneto-electrical Experiments

So far, 2D semiconductors with a superimposed honeycomb potential were investigated with magneto-optical spectroscopy in the far IR and with transport measurements in the Hall geometry. Soibel et al. reported a 2D electron gas in an GaAs/AlGaAs heterostructure in which an array of metallic gates formed a honeycomb lattice with 150 nm unit cell constant.[340] The magneto-resistance showed weak features of the honeycomb potential, increasing with increasing gate voltages. Similar results were reported for alternative GaAs devices, in which the honeycomb potential was obtained by a hexagonal array of holes.[250] With magneto-optical spectroscopy, the energy difference between subsequent Landau states was measured.[15,249] The splitting of the light absorptance peaks (in the meV) region and the fact that the splitting between the Landau states increased sublinearly with the applied magnetic field were attributed to the effect of the superimposed honeycomb potential. Very similar results were reported for a two-dimensional electron gas residing in GaAs modulated by an array of electron-attractive gates by Singha et al.[15] The splitting between subsequent Landau states was measured, and more importantly, the clear degeneracy breaking of a single Landau state due to Coulomb interactions was observed, with a Hubbard gap in the 5 meV region. The same group of researchers reported results that point more explicitly to the existence of Dirac carriers. Using resonant inelastic light scattering (RILS), band transitions in the lowest conduction bands of honeycomb GaAs could be studied;[18] see Figure 15. The authors attribute features in the RILS spectrum to transitions between the M points in the lowest Dirac cone, while higher-energy transitions were attributed to transitions between the lowest Dirac cone and higher bands.

### Prospects for Semiconductors with Massless Dirac Carriers

Despite all these efforts, strong evidence for the existence and action of massless Dirac electrons in 2D honeycomb semiconductors has not yet been provided. The modulation of the effect of the arrays of metallic gates in the region of the electron gas is rather weak and is estimated to be in the 10 meV range. Moreover, the translation vector had magnitudes in the 100 nm range, resulting in Dirac cones with a weak energy-wave vector dispersion. It is also clear that detection of the local density of states and energy-resolved wave function mapping with scanning tunneling microscopy and spectroscopy can provide more direct evidence for Dirac-type band structures than nonlocal methods (see section 7), especially in the early phases of the research and development.

Looking to the future of this field, it is worth mentioning that modern lithographic techniques and state-of-the art templating with coblock polymers allow the preparation of III−V semiconductors with a honeycomb periodicity in the 30 nm range. This automatically results in more dispersive Dirac cones, now over an energy scale in the tens of millielectron volts. Furthermore, self-assembled nanocrystal honeycomb structures are predicted to have Dirac cones with widths in the 100 meV range, provided that the nanocrystal sites are well coupled.[20] This opens new perspectives for the creation of semiconductors in which electron and/or hole excitations are robust massless Dirac carriers. Understanding that intrinsic spin−orbit coupling is strong in these systems, flawless honeycomb semiconductors with a small periodicity open an entire new materials field in which the band structure can be modulated by the nanoscale geometry, interactions, and spin−orbit coupling.[21,41] Strong spin−orbit coupling could open topological gaps in the 30 meV range, offering quantum spin Hall edge states for technology under affordable conditions.

## AUTHOR INFORMATION


### Corresponding Author

**Daniel Vanmaekelbergh** − *Condensed Matter and Interfaces, Debye Institute of Nanomaterial Science, University of Utrecht, 3584 CC Utrecht, The Netherlands;* orcid.org/0000-0002-3535-8366; Email: d.vanmaekelbergh@uu.nl

### Authors

**Saoirsé E. Freeney** − *Condensed Matter and Interfaces, Debye Institute of Nanomaterial Science, University of Utrecht, 3584 CC Utrecht, The Netherlands*

**Marlou R. Slot** − *Condensed Matter and Interfaces, Debye Institute of Nanomaterial Science, University of Utrecht, 3584 CC Utrecht, The Netherlands;* orcid.org/0000-0003-0770-0125

**Thomas S. Gardenier** − *Condensed Matter and Interfaces, Debye Institute of Nanomaterial Science, University of Utrecht, 3584 CC Utrecht, The Netherlands;* orcid.org/0000-0002-5100-7996

**Ingmar Swart** − *Condensed Matter and Interfaces, Debye Institute of Nanomaterial Science, University of Utrecht, 3584 CC Utrecht, The Netherlands;* orcid.org/0000-0003-3201-7301

Complete contact information is available at: https://pubs.acs.org/10.1021/acsnanoscienceau.1c00054


### Notes

The authors declare no competing financial interest.

## REFERENCES


(1) Keimer, B.; Moore, J. E. The physics of quantum materials. *Nat. Phys.* **2017**, *13*, 1045−1055.

(2) Qi, X. L.; Zhang, S. C. The quantum spin Hall effect and topological insulators. *Phys. Today* **2010**, *63*, 33−38.

(3) Von Klitzing, K. The quantized Hall effect. *Rev. Mod. Phys.* **1986**, *58*, 519−531.

(4) Stormer, H. L. Nobel Lecture: The fractional quantum Hall effect. *Rev. Mod. Phys.* **1999**, *71*, 875−889.

(5) Behnia, K. High-temperature superconductivity - Charged with smuggling heat. *Nature* **2001**, *414*, 696−697.

(6) Chen, H. D.; Vafek, O.; Yazdani, A.; Zhang, S. C. Pair density wave in the pseudogap state of high temperature superconductors. *Phys. Rev. Lett.* **2004**, *93*, 187002.
(7) Anderson, P. W.; et al. The physics behind high-temperature superconducting cuprates: the 'plain vanilla' version of RVB. *J. Phys.-Condes. Matter* **2004**, *16*, R755−R769.
(8) Fischer, ÿ.; Kugler, M.; Maggio-Aprile, I.; Berthod, C.; Renner, C. Scanning tunneling spectroscopy of high-temperature superconductors. *Rev. Mod. Phys.* **2007**, *79*, 353−419.
(9) Drozdov, A. P.; Eremets, M. I.; Troyan, I. A.; Ksenofontov, V.; Shylin, S. I. Conventional superconductivity at 203 K at high pressures in the sulfur hydride system. *Nature* **2015**, *525*, 73.
(10) Chen, C.; et al. Atomic line defects and zero-energy end states in monolayer Fe(Te,Se) high-temperature superconductors. *Nat. Phys.* **2020**, *16*, 536.
(11) Murray, C. B.; Kagan, C. R.; Bawendi, M. G. Synthesis and characterization of monodisperse nanocrystals and close-packed nanocrystal assemblies. *Annu. Rev. Mater. Sci.* **2000**, *30*, 545−610.
(12) Alivisatos, A. P. Perspectives on the physical chemistry of semiconductor nanocrystals. *J. Phys. Chem.* **1996**, *100*, 13226−13239.
(13) Brus, L. E. Electronic and optical properties of semiconductor nanocrystals: From molecules to bulk crystals. *NATO ASI Ser., Ser. E* **1994**, *260*, 433−448.
(14) Gibertini, M.; et al. Engineering artificial graphene in a two-dimensional electron gas. *Phys. Rev. B* **2009**, *79*, 241406.
(15) Singha, A.; et al. Two-Dimensional Mott-Hubbard Electrons in an Artificial Honeycomb Lattice. *Science* **2011**, *332*, 1176−1179.
(16) Scarabelli, D.; et al. Fabrication of artificial graphene in a GaAs quantum heterostructure. *J. Vac. Sci. Technol. B* **2015**, *33*, 06FG03.
(17) Du, L. J.; et al. Emerging many-body effects in semiconductor artificial graphene with low disorder. *Nat. Commun.* **2018**, *9*, 3299.
(18) Wang, S.; et al. Observation of Dirac bands in artificial graphene in small-period nanopatterned GaAs quantum wells. *Nat. Nanotechnol.* **2018**, *13*, 29018.
(19) Kalesaki, E.; Evers, W. H.; Allan, G.; Vanmaekelbergh, D.; Delerue, C. Electronic structure of atomically coherent square semiconductor superlattices with dimensionality below two. *Phys. Rev. B* **2013**, *88*, 115431.
(20) Kalesaki, E.; et al. Dirac Cones, Topological Edge States, and Nontrivial Flat Bands in Two-Dimensional Semiconductors with a Honeycomb Nanogeometry. *Physical Review X* **2014**, *4*, 011010.
(21) Beugeling, W.; et al. Topological states in multi-orbital HgTe honeycomb lattices. *Nat. Commun.* **2015**, *6*, 6316.
(22) Xu, C. K.; Moore, J. E. Stability of the quantum spin Hall effect: Effects of interactions, disorder, and Z(2) topology. *Phys. Rev. B* **2006**, *73*, 045322.
(23) Moore, J. E. The birth of topological insulators. *Nature* **2010**, *464*, 194−198.
(24) Moore, J. E. TOPOLOGICAL INSULATORS. *Ieee Spectrum* **2011**, *48*, 38−57.
(25) Hor, Y. S.; et al. p-type Bi2Se3 for topological insulator and low-temperature thermoelectric applications. *Phys. Rev. B* **2009**, *79*, 195208.
(26) Zhang, H. J.; et al. Topological insulators in Bi2Se3, Bi2Te3 and Sb2Te3 with a single Dirac cone on the surface. *Nat. Phys.* **2009**, *5*, 438−442.
(27) Cheng, P.; et al. Landau Quantization of Topological Surface States in Bi2Se3. *Phys. Rev. Lett.* **2010**, *105*, 076801.
(28) Hor, Y. S.; et al. Superconductivity in CuxBi2Se3 and its Implications for Pairing in the Undoped Topological Insulator. *Phys. Rev. Lett.* **2010**, *104*, 057001.
(29) Hsieh, T. H.; Fu, L. Majorana Fermions and Exotic Surface Andreev Bound States in Topological Superconductors: Application to CuxBi2Se3. *Phys. Rev. Lett.* **2012**, *108*, 107005.
(30) Yazyev, O. V.; Kioupakis, E.; Moore, J. E.; Louie, S. G. Quasiparticle effects in the bulk and surface-state bands of Bi2Se3 and Bi2Te3 topological insulators. *Phys. Rev. B* **2012**, *85*, 161101.
(31) Zhang, T.; Levy, N.; Ha, J.; Kuk, Y.; Stroscio, J. A. Scanning tunneling microscopy of gate tunable topological insulator Bi2Se3 thin films. *Phys. Rev. B* **2013**, *87*, 115410.
(32) Wang, X. X.; Chiang, T. C. Topological states in Bi2Se3 surfaces created by cleavage within a quintuple layer: Analysis in terms of the Shockley criterion. *Phys. Rev. B* **2014**, *89*, 125109.
(33) Kung, H. H.; et al. Observation of chiral surface excitons in a topological insulator Bi2Se3. *Proc. Natl. Acad. Sci. U.S.A.* **2019**, *116*, 4006−4011.
(34) Bernevig, B. A.; Hughes, T. L.; Zhang, S.-C. Quantum spin Hall effect and topological phase transition in HgTe quantum wells. *Science* **2006**, *314*, 1757−1761.
(35) Bruene, C.; et al. Quantum Hall Effect from the Topological Surface States of Strained Bulk HgTe. *Phys. Rev. Lett.* **2011**, *106*, 126803.
(36) Beugeling, W.; Liu, C. X.; Novik, E. G.; Molenkamp, L. W.; Smith, C. M. Reentrant topological phases in Mn-doped HgTe quantum wells. *Phys. Rev. B* **2012**, *85*, 195304.
(37) Drozdov, I. K.; et al. One-dimensional topological edge states of bismuth bilayers. *Nat. Phys.* **2014**, *10*, 664−669.
(38) Li, J.; et al. Topological superconductivity induced by ferromagnetic metal chains. *Phys. Rev. B* **2014**, *90*, 235433.
(39) Bradlyn, B.; et al. Topological quantum chemistry. *Nature* **2017**, *547*, 298−305.
(40) Cano, J.; et al. Building blocks of topological quantum chemistry: Elementary band representations. *Phys. Rev. B* **2018**, *97*, 035139.
(41) Kane, C. L.; Mele, E. J. Quantum spin Hall effect in graphene. *Phys. Rev. Lett.* **2005**, *95*, 226801.
(42) Kane, C. L.; Mele, E. J. Z(2) topological order and the quantum spin Hall effect. *Phys. Rev. Lett.* **2005**, *95*, 146802.
(43) Fu, L.; Kane, C. L. Topological insulators with inversion symmetry. *Phys. Rev. B* **2007**, *76*, 045302.
(44) Fu, L.; Kane, C. L.; Mele, E. J. Topological insulators in three dimensions. *Phys. Rev. Lett.* **2007**, *98*, 106803.
(45) Hasan, M. Z.; Kane, C. L. Colloquium: Topological insulators. *Rev. Mod. Phys.* **2010**, *82*, 3045−3067.
(46) Hasan, M. Z.; Moore, J. E. Three-Dimensional Topological Insulators. *Annu. Rev. Condens. Matter Phys.* **2011**, *2*, 55−78.
(47) Siegel, D. A.; et al. Many-body interactions in quasi-freestanding graphene. *Proc. Natl. Acad. Sci. U.S.A.* **2011**, *108*, 11365−11369.
(48) Bhimanapati, G. R.; et al. Recent Advances in Two-Dimensional Materials beyond Graphene. *ACS Nano* **2015**, *9*, 11509−11539.
(49) Wu, C. J.; Bergman, D.; Balents, L.; Sarma, S. D. Flat bands and Wigner crystallization in the Honeycomb optical lattice. *Phys. Rev. Lett.* **2007**, *99*, 070401.
(50) Sau, J. D.; Tewari, S.; Lutchyn, R. M.; Stanescu, T. D.; Das Sarma, S. Non-Abelian quantum order in spin-orbit-coupled semiconductors: Search for topological Majorana particles in solid-state systems. *Phys. Rev. B* **2010**, *82*, 214509.
(51) Sun, K.; Gu, Z.; Katsura, H.; Das Sarma, S. Nearly Flatbands with Nontrivial Topology. *Phys. Rev. Lett.* **2011**, *106*, 236803.
(52) Young, S. M.; et al. Theoretical investigation of the evolution of the topological phase of Bi(2)Se(3) under mechanical strain. *Phys. Rev. B* **2011**, *84*, 085106.
(53) Luo, J. W.; Zunger, A. Design principles and coupling mechanisms in the 2D quantum well topological insulator HgTe/CdTe. *Phys. Rev. Lett.* **2010**, *105*, 176805.
(54) Novoselov, K. S.; et al. Two-dimensional gas of massless Dirac fermions in graphene. *Nature* **2005**, *438*, 197−200.
(55) Boneschanscher, M. P.; et al. Quantitative Atomic Resolution Force Imaging on Epitaxial Graphene with Reactive and Nonreactive AFM. *Probes. Acs Nano* **2012**, *6*, 10216−10221.
(56) van der Lit, J.; et al. Suppression of electron-vibron coupling in graphene nanoribbons contacted via a single atom. *Nat. Commun.* **2013**, *4*, 2023.

(57) van der Heijden, N. J.; et al. Recognizing nitrogen dopant atoms in graphene using atomic force microscopy. *Phys. Rev. B* **2016**, *93*, 245430.
(58) Hamalainen, S. K.; et al. Structure and local variations of the graphene moire on Ir(111). *Phys. Rev. B* **2013**, *88*, 201406.
(59) Sun, Z.; et al. Topographic and electronic contrast of the graphene moire on Ir(111) probed by scanning tunneling microscopy and noncontact atomic force microscopy. *Phys. Rev. B* **2011**, *83*, 081415.
(60) Jarvinen, P.; et al. Molecular Self-Assembly on Graphene on SiO2 and h-BN Substrates. *Nano Lett.* **2013**, *13*, 3199−3204.
(61) Drost, R.; et al. Electronic States at the Graphene-Hexagonal Boron Nitride Zigzag Interface. *Nano Lett.* **2014**, *14*, 5128−5132.
(62) Zhang, Y.; et al. Giant phonon-induced conductance in scanning tunnelling spectroscopy of gate-tunable graphene. *Nat. Phys.* **2008**, *4*, 627−630.
(63) Zhang, Y.; Brar, V. W.; Girit, C.; Zettl, A.; Crommie, M. F. Origin of spatial charge inhomogeneity in graphene. *Nat. Phys.* **2009**, *5*, 722−726.
(64) Wang, Y.; et al. Mapping Dirac quasiparticles near a single Coulomb impurity on graphene. *Nat. Phys.* **2012**, *8*, 653−657.
(65) Wang, Y.; et al. Observing Atomic Collapse Resonances in Artificial Nuclei on Graphene. *Science* **2013**, *340*, 734−737.
(66) Schulz, F.; et al. Precursor Geometry Determines the Growth Mechanism in Graphene Nanoribbons. *J. Phys. Chem. C* **2017**, *121*, 2896−2904.
(67) Zhang, X.; et al. Experimentally Engineering the Edge Termination of Graphene Nanoribbons. *ACS Nano* **2013**, *7*, 198−202.
(68) Cai, J.; et al. Atomically precise bottom-up fabrication of graphene nanoribbons. *Nature* **2010**, *466*, 470−473.
(69) Sode, H.; et al. Electronic band dispersion of graphene nanoribbons via Fourier-transformed scanning tunneling spectroscopy. *Phys. Rev. B* **2015**, *91*, 045429.
(70) Ruffieux, P.; et al. On-surface synthesis of graphene nanoribbons with zigzag edge topology. *Nature* **2016**, *531*, 489−492.
(71) Wang, S. Y.; et al. Giant edge state splitting at atomically precise graphene zigzag edges. *Nat. Commun.* **2016**, *7*, 11507.
(72) Talirz, L.; et al. On-Surface Synthesis and Characterization of 9-Atom Wide Armchair Graphene Nanoribbons. *ACS Nano* **2017**, *11*, 1380−1388.
(73) van der Lit, J.; Jacobse, P. H.; Vanmaekelbergh, D.; Swart, I. Bending and buckling of narrow armchair graphene nanoribbons via STM manipulation. *New J. Phys.* **2015**, *17*, 053013.
(74) Ijas, M.; et al. Electronic states in finite graphene nanoribbons: Effect of charging and defects. *Phys. Rev. B* **2013**, *88*, 075429.
(75) Tao, C.; et al. Spatially resolving edge states of chiral graphene nanoribbons. *Nat. Phys.* **2011**, *7*, 616−620.
(76) Chen, Y.-C.; et al. Tuning the Band Gap of Graphene Nanoribbons Synthesized from Molecular Precursors. *ACS Nano* **2013**, *7*, 6123−6128.
(77) Konig, M.; et al. Quantum spin hall insulator state in HgTe quantum wells. *Science* **2007**, *318*, 766−770.
(78) Babbush, R.; Love, P. J.; Aspuru-Guzik, A. Adiabatic Quantum Simulation of Quantum Chemistry. *Sci. Rep* **2015**, *4*, 06603.
(79) Bloch, I.; Dalibard, J.; Nascimbene, S. Quantum simulations with ultracold quantum gases. *Nat. Phys.* **2012**, *8*, 267−276.
(80) Zhang, J. F.; Yung, M. H.; Laflamme, R.; Aspuru-Guzik, A.; Baugh, J. Digital quantum simulation of the statistical mechanics of a frustrated magnet. *Nat. Commun.* **2012**, *3*, 1860.
(81) Choi, J. Y.; et al. QUANTUM SIMULATION Exploring the many-body localization transition in two dimensions. *Science* **2016**, *352*, 1547−1552.
(82) Dauphin, A.; Muller, M.; Martin-Delgado, M. A. Quantum simulation of a topological Mott insulator with Rydberg atoms in a Lieb lattice. *Phys.Rev.A* **2016**, *93*, 043611.
(83) Bercioux, D.; Otte, S. Quantum Simulation Solid-state platforms. *Nat. Phys.* **2017**, *13*, 628−629.
(84) Gross, C.; Bloch, I. Quantum simulations with ultracold atoms in optical lattices. *Science* **2017**, *357*, 995−1001.
(85) Barthelemy, P.; Vandersypen, L. M. K. Quantum Dot Systems: a versatile platform for quantum simulations. *Annalen Der Physik* **2013**, *525*, 808−826.
(86) Ward, N. J.; Kassal, I.; Aspuru-Guzik, A. Preparation of many-body states for quantum simulation. *J. Chem. Phys.* **2009**, *130*, 194105.
(87) Schmied, R.; Wesenberg, J. H.; Leibfried, D. Quantum simulation of the hexagonal Kitaev model with trapped ions. *New J. Phys.* **2011**, *13*, 115011.
(88) Schaetz, T.; Monroe, C. R.; Esslinger, T. Focus on quantum simulation. *New J. Phys.* **2013**, *15*, 085009.
(89) Babbush, R.; et al. Exponentially more precise quantum simulation of fermions in second quantization. *New J. Phys.* **2016**, *18*, 033032.
(90) Hensgens, T.; et al. Quantum simulation of a Fermi-Hubbard model using a semiconductor quantum dot array. *Nature* **2017**, *548*, 70.
(91) O'Malley, P. J. J.; et al. Scalable Quantum Simulation of Molecular Energies. *Physical Review X* **2016**, *6*, 031007.
(92) Feynman, R. P. SIMULATING PHYSICS WITH COMPUTERS. *International Journal of Theoretical Physics* **1982**, *21*, 467−488.
(93) Feynman, R. P. Quantum-Mechanical Computers. *J. Opt. Soc. Am. B-Opt. Phys.* **1984**, *1*, 464.
(94) Peng, X. N.; et al. Visualizing designer quantum states in stable macrocycle quantum corrals. *Nat. Commun.* **2021**, *12*, 5895.
(95) Telychko, M.; et al. Ultrahigh-yield on-surface synthesis and assembly of circumcoronene into a chiral electronic Kagome-honeycomb lattice. *Science Advances* **2021**, *7*, abf0269.
(96) Barth, J. V.et al. Engineering interfacial quantum states and electronic landscapes by molecular nanoarchitectures. *arXiv (Mesoscale and Nanoscale Physics)*, July 21, **2021**, 2107.10141, ver. 1.
(97) Hou, J.-M.; Yang, W.-X. Next-nearest-neighbor-tunneling-induced symmetry breaking of Hofstadter's butterfly spectrum for ultracold atoms on the honeycomb lattice. *Phys. Lett. A* **2009**, *373*, 2774.
(98) Eiguren, A.; et al. Role of bulk and surface phonons in the decay of metal surface states. *Phys. Rev. Lett.* **2002**, *88*, 066805.
(99) Tsai, W. F.; Fang, C.; Yao, H.; Hu, J. P. Interaction-driven topological and nematic phases on the Lieb lattice. *New J. Phys.* **2015**, *17*, 055016.
(100) Castro, E. V.; et al. Topological Fermi Liquids from Coulomb Interactions in the Doped Honeycomb Lattice. *Phys. Rev. Lett.* **2011**, *107*, 106402.
(101) Wen, J.; Rueegg, A.; Wang, C. C. J.; Fiete, G. A. Interaction-driven topological insulators on the kagome and the decorated honeycomb lattices. *Phys. Rev. B* **2010**, *82*, 075125.
(102) Rachel, S.; Le Hur, K. Topological insulators and Mott physics from the Hubbard interaction. *Phys. Rev. B* **2010**, *82*, 075106.
(103) Rachel, S. Interacting topological insulators: a review. *Rep. Prog. Phys.* **2018**, *81*, 116501.
(104) Weeks, C.; Hu, J.; Alicea, J.; Franz, M.; Wu, R. Engineering a Robust Quantum Spin Hall State in Graphene via Adatom Deposition. *Physical Review X* **2011**, *1*, 021001.
(105) Volkov, A. F.; Magnee, P. H. C.; Vanwees, B. J.; Klapwijk, T. M. PROXIMITY AND JOSEPHSON EFFECTS IN SUPERCONDUCTOR 2-DIMENSIONAL ELECTRON-GAS PLANAR JUNCTIONS. *Physica C-Superconductivity and Its Applications* **1995**, *242*, 261−266.
(106) Kopnin, N. B.; Melnikov, A. S. Proximity-induced superconductivity in two-dimensional electronic systems. *Phys. Rev. B* **2011**, *84*, 064524.
(107) Dai, W. Q.; et al. Proximity-effect-induced Superconducting Gap in Topological Surface States - A Point Contact Spectroscopy Study of NbSe2/Bi2Se3 Superconductor-Topological Insulator Heterostructures. *Sci. Rep* **2017**, *7*, 7631.


https://doi.org/10.1021/acsnanoscienceau.1c00054
*ACS Nanosci. Au* 2022, 2, 198−224

(108) Polini, M.; Guinea, F.; Lewenstein, M.; Manoharan, H. C.; Pellegrini, V. Artificial honeycomb lattices for electrons, atoms and photons. *Nat. Nanotechnol.* **2013**, *8*, 625−633.
(109) Bloch, I. Exploring quantum matter with ultracold atoms in optical lattices. *Journal of Physics B-Atomic Molecular and Optical Physics* **2005**, *38*, S629−S643.
(110) Bloch, I. Quantum gases in opotical lattices. *Phys. World* **2004**, *17*, 25−29.
(111) Bloch, I. Ultracold quantum gases in optical lattices. *Nat. Phys.* **2005**, *1*, 23−30.
(112) Grusdt, F.; Li, T.; Bloch, I.; Demler, E. Tunable spin-orbit coupling for ultracold atoms in two-dimensional optical lattices. *Phys.Rev.A* **2017**, *95*, 063617.
(113) Goldman, N.; Urban, D. F.; Bercioux, D. Topological phases for fermionic cold atoms on the Lieb lattice. *Phys.Rev.A* **2011**, *83*, 063601.
(114) Bloch, I.; Rosch, A. Exploring strongly correlated quantum many-body systems with ultracold atoms in optical lattices. *Phys. Status Solidi B-Basic Solid State Phys.* **2010**, *247*, 530−536.
(115) Barmettler, P.; et al. Quantum many-body dynamics of coupled double-well superlattices. *Phys.Rev.A* **2008**, *78*, 012330.
(116) Bloch, I.; Dalibard, J.; Zwerger, W. Many-body physics with ultracold gases. *Rev. Mod. Phys.* **2008**, *80*, 885−964.
(117) Karzig, T.; Bardyn, C.-E.; Lindner, N. H.; Refael, G. Topological Polaritons. *Physical Review X* **2015**, *5*, 031001.
(118) Nalitov, A. V.; Solnyshkov, D. D.; Malpuech, G. Polariton Z Topological Insulator. *Phys. Rev. Lett.* **2015**, *114*, 116401.
(119) Baboux, F.; et al. Measuring topological invariants from generalized edge states in polaritonic quasicrystals. *Phys. Rev. B* **2017**, *95*, 161114.
(120) Chi, Z. M.; Guo, X. Y.; Wang, Z. J. Topological phase transition of two-dimensional topological polaritons. *Int. J. Mod. Phys. B* **2017**, *31*, 1750070.
(121) Gulevich, D. R.; Yudin, D.; Skryabin, D. V.; Iorsh, I. V.; Shelykh, I. A. Exploring nonlinear topological states of matter with exciton-polaritons: Edge solitons in kagome lattice. *Sci. Rep* **2017**, *7*, 1780.
(122) Klembt, S.; et al. Exciton-polariton topological insulator. *Nature* **2018**, *562*, 552−556.
(123) Li, C. Y.; et al. Lieb polariton topological insulators. *Phys. Rev. B* **2018**, *97*, 081103.
(124) Solnyshkov, D. D.; Bleu, O.; Malpuech, G. Topological optical isolator based on polariton graphene. *Appl. Phys. Lett.* **2018**, *112*, 031106.
(125) Suchomel, H.; et al. Platform for Electrically Pumped Polariton Simulators and Topological Lasers. *Phys. Rev. Lett.* **2018**, *121*, 257402.
(126) Zhang, C. Y.; Wang, Y. X.; Zhang, W. F. Topological phase transition with p orbitals in the exciton-polariton honeycomb lattice. *J. Phys.-Condes. Matter* **2019**, *31*, 335403.
(127) Bajoni, D.; et al. Exciton polaritons in two-dimensional photonic crystals. *Phys. Rev. B* **2009**, *80*, 201308.
(128) Galbiati, M.; et al. Polariton Condensation in Photonic Molecules. *Phys. Rev. Lett.* **2012**, *108*, 126403.
(129) Tanese, D.; et al. Fractal Energy Spectrum of a Polariton Gas in a Fibonacci Quasiperiodic Potential. *Phys. Rev. Lett.* **2014**, *112*, 146404.
(130) Amo, A.; Bloch, J. Exciton-polaritons in lattices: A non-linear photonic simulator. *Comptes Rendus Physique* **2016**, *17*, 934−945.
(131) Lumer, Y.; Plotnik, Y.; Rechtsman, M. C.; Segev, M. Self-Localized States in Photonic Topological Insulators. *Phys. Rev. Lett.* **2013**, *111*, 243905.
(132) Lumer, Y., Rechtsman, M. C., Plotnik, Y., Segev, M. 2013 Conference on Lasers and Electro-Optics Conference on Lasers and Electro-Optics, 2013.
(133) Rechtsman, M. C.; et al. Topological Creation and Destruction of Edge States in Photonic Graphene. *Phys. Rev. Lett.* **2013**, *111*, 103901.
(134) Bandres, M. A., Rechtsman, M. C., Szameit, A., Segev, M. 2014 Conference on Lasers and Electro-Optics Conference on Lasers and Electro-Optics, 2014.
(135) Guzman-Silva, D.; et al. Experimental observation of bulk and edge transport in photonic Lieb lattices. *New J. Phys.* **2014**, *16*, 063061.
(136) Plotnik, Y.; et al. Observation of unconventional edge states in 'photonic graphene'. *Nat. Mater.* **2014**, *13*, 57−62.
(137) Plotnik, Y. et al. 2014 Conference on Lasers and Electro-Optics Conference on Lasers and Electro-Optics, 2014.
(138) Jacqmin, T.; et al. Direct Observation of Dirac Cones and a Flatband in a Honeycomb Lattice for Polaritons. *Phys. Rev. Lett.* **2014**, *112*, 116402.
(139) Milicevic, M.; et al. Edge states in polariton honeycomb lattices. *2d Materials* **2015**, *2*, 034012.
(140) Bandres, M. A., Rechtsman, M. C., Segev, M. 2015 Conference on Lasers and Electro-Optics Conference on Lasers and Electro-Optics, 2015.
(141) Plotnik, Y.; et al. Analogue of Rashba pseudo-spin-orbit coupling in photonic lattices by gauge field engineering. *Phys. Rev. B* **2016**, *94*, 020301.
(142) Munoz-Matutano, G.; et al. Emergence of quantum correlations from interacting fibre-cavity polaritons. *Nat. Mater.* **2019**, *18*, 213.
(143) Rechtsman, M. C. et al. 2015 Conference on Lasers and Electro-Optics Conference on Lasers and Electro-Optics, 2015.
(144) Rechtsman, M. C.; et al. Topological protection of photonic path entanglement. *Optica* **2016**, *3*, 925−930.
(145) Rechtsman, M. C.; et al. Photonic Floquet topological insulators. *Nature* **2013**, *496*, 196−200.
(146) Lumer, Y.; Rechtsman, M. C.; Plotnik, Y.; Segev, M. Instability of bosonic topological edge states in the presence of interactions. *Phys.Rev.A* **2016**, *94*, 021801.
(147) Hanson, R.; Kouwenhoven, L. P.; Petta, J. R.; Tarucha, S.; Vandersypen, L. M. K. Spins in few-electron quantum dots. *Rev. Mod. Phys.* **2007**, *79*, 1217−1265.
(148) Liu, X. L.; Hug, D.; Vandersypen, L. M. K. Gate-defined graphene double quantum dot and excited state spectroscopy. *Nano Lett.* **2010**, *10*, 1623−1627.
(149) Rudner, M. S.; Vandersypen, L. M.; Vuletic, V.; Levitov, L. S. Generating entanglement and squeezed states of nuclear spins in quantum dots. *Phys. Rev. Lett.* **2011**, *107*, 206806.
(150) Schuetz, M. J. A.; et al. Quantum simulation and optimization in hot quantum networks. *Phys. Rev. B* **2019**, *99*, 241302.
(151) Binnig, G.; Rohrer, H.; Gerber, C.; Weibel, E. SURFACE STUDIES BY SCANNING TUNNELING MICROSCOPY. *Phys. Rev. Lett.* **1982**, *49*, 57−61.
(152) Binnig, G.; Rohrer, H. SCANNING TUNNELING MICROSCOPY - FROM BIRTH TO ADOLESCENCE. *Rev. Mod. Phys.* **1987**, *59*, 615−625.
(153) Wiesendanger, R. *Scanning probe microscopy and spectroscopy. Methods and applications*; Cambridge University Press, 1994.
(154) Reed, M. A. *QUANTUM DOT RESONANT TUNNELING SPECTROSCOPY* **1989**, *29*, 267.
(155) Davis, L. C.; Everson, M. P.; Jaklevic, R. C.; Shen, W. D. THEORY OF THE LOCAL DENSITY OF SURFACE-STATES ON A METAL - COMPARISON WITH SCANNING TUNNELING SPECTROSCOPY OF A AU(111) SURFACE. *Phys. Rev. B* **1991**, *43*, 3821−3830.
(156) Ashoori, R. C.; Lebens, J. A.; Bigelow, N. P.; Silsbee, R. H. ENERGY GAPS OF THE 2-DIMENSIONAL ELECTRON-GAS EXPLORED WITH EQUILIBRIUM TUNNELING SPECTROSCOPY. *Phys. Rev. B* **1993**, *48*, 4616−4628.
(157) Porath, D.; Levi, Y.; Tarabiah, M.; Millo, O. Tunneling spectroscopy of isolated C-60 molecules in the presence of charging effects. *Phys. Rev. B* **1997**, *56*, 9829−9833.
(158) Legrand, B.; et al. Scanning tunneling microscopy and scanning tunneling spectroscopy of self assembled InAs quantum dots. *Appl. Phys. Lett.* **1998**, *73*, 96−98.


https://doi.org/10.1021/acsnanoscienceau.1c00054
*ACS Nanosci. Au* 2022, 2, 198−224

(159) Kliewer, J.; Berndt, R. Scanning tunneling spectroscopy of Na on Cu(111). *Phys. Rev. B* **2001**, *65*, 035412.
(160) Klusek, Z.; et al. Graphene on gold: Electron density of states studies by scanning tunneling spectroscopy. *Appl. Phys. Lett.* **2009**, *95*, 113114.
(161) Swart, I.; Liljeroth, P.; Vanmaekelbergh, D. Scanning probe microscopy and spectroscopy of colloidal semiconductor nanocrystals and assembled structures. *Chem. Rev.* **2016**, *116*, 11181−11219.
(162) Liljeroth, P.; Repp, J.; Meyer, G. Current-induced hydrogen tautomerization and conductance switching of naphthalocyanine molecules. *Science* **2007**, *317*, 1203−1206.
(163) Gross, L.; et al. Measuring the Charge State of an Adatom with Noncontact Atomic Force Microscopy. *Science* **2009**, *324*, 1428−1431.
(164) Pavlicek, N.; Swart, I.; Niedenfuehr, J.; Meyer, G.; Repp, J. Symmetry Dependence of Vibration-Assisted Tunneling. *Phys. Rev. Lett.* **2013**, *110*, 136101.
(165) Uhlmann, C.; Swart, I.; Repp, J. Controlling the Orbital Sequence in Individual Cu-Phthalocyanine Molecules. *Nano Lett.* **2013**, *13*, 777−780.
(166) Bakkers, E.; et al. Shell-tunneling Spectroscopy of the single-particle energy levels of insulating quantum dots. *Nano Lett.* **2001**, *1*, 551−556.
(167) Shockley, W. On the surface states associated with a periodic potential. *Phys. Rev.* **1939**, *56*, 317−323.
(168) Tamm, I. About a possible type of electron binding on crystal surfaces. *Z. Physik* **1932**, *76*, 849−850.
(169) Tamm, I. About the work function of electrons from metals. *Z. Physik* **1932**, *77*, 774−777.
(170) Goodwin, E. T. Electronic states at the surfaces of crystals I. The approximation of nearly free electrons. *Math. Proc. Camb. Phil. Soc.* **1939**, *35*, 205−220.
(171) Goodwin, E. T. Electronic states at the surfaces of crystals II. The approximation of tight binding: Finite linear chain of atoms. *Proceedings of the Cambridge Philosophical Society* **1939**, *35*, 221−231.
(172) Goodwin, E. T. Electronic states at the surfaces of crystals IV. The activation of adsorbed atoms by surface electrons. *Math. Proc. Camb. Phil. Soc.* **1939**, *35*, 474−484.
(173) Unal, A. A.; et al. Hybridization between the unoccupied Shockley surface state and bulk electronic states on Cu(111). *Phys. Rev. B* **2011**, *84*, 073107.
(174) Crommie, M. F.; Lutz, C. P.; Eigler, D. M. IMAGING STANDING WAVES IN A 2-DIMENSIONAL ELECTRON-GAS. *Nature* **1993**, *363*, 524−527.
(175) Baumberger, F.; Greber, T.; Osterwalder, J. Fermi surfaces of the two-dimensional surface states on vicinal Cu(111). *Phys. Rev. B* **2001**, *64*, 195411.
(176) Courths, R.; Lau, M.; Scheunemann, T.; Gollisch, H.; Feder, R. From the Shockley surface state on Cu(111) to sp-like surface resonances on Cu3Au(111). *Phys. Rev. B* **2001**, *63*, 195110.
(177) Kevan, S. D. EVIDENCE FOR A NEW BROADENING MECHANISM IN ANGLE-RESOLVED PHOTOEMISSION FROM CU(111). *Phys. Rev. Lett.* **1983**, *50*, 526−529.
(178) Everson, M. P.; Davis, L. C.; Jaklevic, R. C.; Shen, W. EFFECTS OF SURFACE-FEATURES UPON THE AU(111) SURFACE-STATE LOCAL DENSITY OF STATES STUDIED WITH SCANNING TUNNELING SPECTROSCOPY. *J. Vac. Sci. Technol. B* **1991**, *9*, 891−896.
(179) Barke, I.; Hovel, H. Confined Shockley surface states on the (111) facets of gold clusters. *Phys. Rev. Lett.* **2003**, *90*, 166801.
(180) Nicholls, J. M.; Salvan, F.; Reihl, B. SURFACE-STATES OF ORDERED AU, AG, AND CU OVERLAYERS ON SI(111) STUDIED BY INVERSE PHOTOEMISSION. *Phys. Rev. B* **1986**, *34*, 2945−2948.
(181) Everson, M. P.; Davis, L. C.; Jaklevic, R. C. Effects of Surface-Features upon the Au(111) Surface-State Local Density of States Studied with Scanning Tunneling Spectroscopy. *J. Vac. Sci. Technol. B* **1991**, *9*, 891−896.
(182) Andreev, T.; Barke, I.; Hovel, H. Adsorbed rare-gas layers on Au(111): Shift of the Shockley surface state studied with ultraviolet photoelectron spectroscopy and scanning tunneling spectroscopy. *Phys. Rev. B* **2004**, *70*, 205426.
(183) Henk, J.; Hoesch, M.; Osterwalder, J.; Ernst, A.; Bruno, P. Spin-orbit coupling in the L-gap surface states of Au(111): spin-resolved photoemission experiments and first-principles calculations. *J. Phys.-Condes. Matter* **2004**, *16*, 7581−7597.
(184) Hoesch, M.; et al. Spin structure of the Shockley surface state on Au(111). *Phys. Rev. B* **2004**, *69*, 241401.
(185) Kroger, J.; Limot, L.; Jensen, H.; Berndt, R.; Johansson, P. Stark effect in Au(111) and Cu(111) surface states. *Phys. Rev. B* **2004**, *70*, 033401.
(186) Muntwiler, M.; et al. Spin- and angle-resolved photoemission spectroscopy study of the Au(111) Shockley surface state. *J. Electron Spectrosc. Relat. Phenom.* **2004**, *137*, 119−123.
(187) Didiot, C.; Fagot-Revurat, Y.; Pons, S.; Kierren, B.; Malterre, D. ARPES and STS investigation of noble metal Shockley states: Confinement in vicinal Au(111) surfaces and self-organized nanostructures. *Surf. Sci.* **2007**, *601*, 4029−4035.
(188) Kowalczyk, P. J.; et al. Investigation of the Shockley surface state on clean and air-exposed Au (111). *Appl. Surf. Sci.* **2008**, *254*, 4572−4576.
(189) Heers, S.; Mavropoulos, P.; Lounis, S.; Zeller, R.; Blugel, S. Lifetime reduction of surface states at Cu, Ag, and Au(111) caused by impurity scattering. *Phys. Rev. B* **2012**, *86*, 125444.
(190) Kim, B.; et al. Spin and orbital angular momentum structure of Cu(111) and Au(111) surface states. *Phys. Rev. B* **2012**, *85*, 195402.
(191) Caravati, S.; et al. Cu(111) and Cu(001) surface electronic states. Comparison between theory and experiment. *Surf. Sci.* **2006**, *600*, 3901−3905.
(192) Heller, E. J.; Crommie, M. F.; Lutz, C. P.; Eigler, D. M. SCATTERING AND ABSORPTION OF SURFACE ELECTRON WAVES IN QUANTUM CORRALS. *Nature* **1994**, *369*, 464−466.
(193) Olsson, F. E.; et al. Localization of the Cu(111) surface state by single Cu adatoms. *Phys. Rev. Lett.* **2004**, *93*, 206803.
(194) Folsch, S.; Hyldgaard, P.; Koch, R.; Ploog, K. H. Quantum confinement in monatomic Cu chains on Cu(111). *Phys. Rev. Lett.* **2004**, *92*, 056803.
(195) Lagoute, J.; Liu, X.; Folsch, S. Link between adatom resonances and the Cu(111) Shockley surface state. *Phys. Rev. Lett.* **2005**, *95*, 136801.
(196) Lagoute, J.; Liu, X.; Folsch, S. Electronic properties of straight, kinked, and branched Cu/Cu(111) quantum wires: A low-temperature scanning tunneling microscopy and spectroscopy study. *Phys. Rev. B* **2006**, *74*, 125410.
(197) Diekhoner, L.; et al. Surface states of cobalt nanoislands on Cu(111). *Phys. Rev. Lett.* **2003**, *90*, 236801.
(198) Barral, M. A.; Weissmann, M.; Llois, A. M. Characterization of the surface states of Co(0001), Co(111), and ultrathin films of Co on Cu(111). *Phys. Rev. B* **2005**, *72*, 125433.
(199) Zhao, X. X.; Mi, Y. M. First-principle calculations on the atomic geometry and electronic states of CO monolayer on cu(001) surface. *Acta Phys.-Chim. Sin.* **2008**, *24*, 127−132.
(200) Rieder, K. H. et al. In *Conference on Atoms and Molecules near Surfaces*; Weiner, J., Feenstra, L., Schmiedmayer, J., Eds.; Journal of Physics Conference Series; 2005; Vol. *19*; pp 175−181.
(201) Bartels, L.; Meyer, G.; Rieder, K. H. Lateral manipulation of single Cu atoms on flat and stepped copper surfaces. *Journal of Vacuum Science & Technology a-Vacuum Surfaces and Films* **1998**, *16*, 1047−1049.
(202) Eigler, D. M.; Schweizer, E. K. Positioning Single Atoms with a Scanning Tunneling Microscope. *Nature* **1990**, *344*, 524−526.
(203) Stroscio, J. A.; Eigler, D. M. Atomic and Molecular Manipulation with the Scanning Tunneling Microscope. *Science* **1991**, *254*, 1319−1326.
(204) Meyer, G.; Bartels, L.; Zophel, S.; Henze, E.; Rieder, K. H. Controlled atom by atom restructuring of a metal surface with the scanning tunneling microscope. *Phys. Rev. Lett.* **1997**, *78*, 1512−1515.


https://doi.org/10.1021/acsnanoscienceau.1c00054
*ACS Nanosci. Au* 2022, 2, 198−224

(205) Bartels, L.; Meyer, G.; Rieder, K. H. Controlled vertical manipulation of single CO molecules with the scanning tunneling microscope: A route to chemical contrast. *Appl. Phys. Lett.* **1997**, *71*, 213−215.
(206) Bartels, L.; Meyer, G.; Rieder, K. H. Basic steps of lateral manipulation of single atoms and diatomic clusters with a scanning tunneling microscope tip. *Phys. Rev. Lett.* **1997**, *79*, 697−700.
(207) Bartels, L.; Meyer, G.; Rieder, K. H. Basic steps involved in the lateral manipulation of single CO molecules and rows of CO molecules. *Chem. Phys. Lett.* **1997**, *273*, 371−375.
(208) Bartels, L.; Meyer, G.; Rieder, K. H. Atomic hop-scotch: different manipulation modes of single Cu atoms on Cu(111). *Chem. Phys. Lett.* **1998**, *285*, 284−287.
(209) Pham, V.; Kanisawa, K.; Folsch, S. Quantum Rings Engineered by Atom Manipulation. *Phys. Rev. Lett.* **2019**, *123*, 066801.
(210) Kumar, A.; Banerjee, K.; Liljeroth, P. Molecular assembly on two-dimensional materials. *Nanotechnology* **2017**, *28*, 082001.
(211) Drost, R.; Ojanen, T.; Harju, A.; Liljeroth, P. Topological states in engineered atomic lattices. *Nat. Phys.* **2017**, *13*, 668.
(212) Robinett, R. W. Energy eigenvalues and periodic orbits for the circular disk or annular infinite well. *Surf. Rev. Lett.* **1998**, *5*, 519−526.
(213) Robinett, R. W. Visualizing the solutions for the circular infinite well in quantum and classical mechanics. *Am. J. Phys.* **1996**, *64*, 440−446.
(214) Slot, M. R.; et al. Experimental realization and characterization of an electronic Lieb lattice. *Nat. Phys.* **2017**, *13*, 672.
(215) Gomes, K. K.; Mar, W.; Ko, W.; Guinea, F.; Manoharan, H. C. Designer Dirac fermions and topological phases in molecular graphene. *Nature* **2012**, *483*, 306−310.
(216) Weeks, C.; Franz, M. Topological insulators on the Lieb and perovskite lattices. *Phys. Rev. B* **2010**, *82*, 085310.
(217) Lieb, E. H. 2 THEOREMS ON THE HUBBARD-MODEL. *Phys. Rev. Lett.* **1989**, *62*, 1201−1204n.
(218) Ma, D.-S.; Xu, Y.; Chiu, C. S.; Regnault, N.; Houck, A. A.; Song, Z.; Bernevig, B. A. Spin-orbit induced toplogicasl flat bands in lineand split graphs of bipartite lattices. *Phys. Rev. Lett.* **2020**, *125*, 266403.
(219) Mukherjee, S.; et al. Observation of a Localized Flat-Band State in a Photonic Lieb Lattice. *Phys. Rev. Lett.* **2015**, *114*, 245504.
(220) Vicencio, R. A.; et al. Observation of Localized States in Lieb Photonic Lattices. *Phys. Rev. Lett.* **2015**, *114*, 245503.
(221) Julku, A.; Peotta, S.; Vanhala, T. I.; Kim, D. H.; Torma, P. Geometric Origin of Superfluidity in the Lieb-Lattice Flat Band. *Phys. Rev. Lett.* **2016**, *117*, 045303.
(222) Xia, S. Q.; et al. Demonstration of flat-band image transmission in optically induced Lieb photonic lattices. *Opt. Lett.* **2016**, *41*, 1435−1438.
(223) Nita, M.; Ostahie, B.; Aldea, A. Spectral and transport properties of the two-dimensional Lieb lattice. *Phys. Rev. B* **2013**, *87*, 125428.
(224) Apaja, V.; Hyrkas, M.; Manninen, M. Flat bands, Dirac cones, and atom dynamics in an optical lattice. *Phys.Rev.A* **2010**, *82*, 041402.
(225) Taie, S.; et al. Coherent driving and freezing of bosonic matter wave in an optical Lieb lattice. *Science Advances* **2015**, *1*, 1500854.
(226) Ozawa, H.; Taie, S.; Ichinose, T.; Takahashi, Y. Interaction-Driven Shift and Distortion of a Flat Band in an Optical Lieb Lattice. *Phys. Rev. Lett.* **2017**, *118*, 175301.
(227) Diebel, F.; Leykam, D.; Kroesen, S.; Denz, C.; Desyatnikov, A. S. Conical Diffraction and Composite Lieb Bosons in Photonic Lattices. *Phys. Rev. Lett.* **2016**, *116*, 183902.
(228) Xia, S. Q.; et al. Unconventional Flatband Line States in Photonic Lieb Lattices. *Phys. Rev. Lett.* **2018**, *121*, 263902.
(229) Whittaker, C. E.; et al. Exciton Polaritons in a Two-Dimensional Lieb Lattice with Spin-Orbit Coupling. *Phys. Rev. Lett.* **2018**, *120*, 097401.
(230) Yang, Z. H.; et al. Circuit quantum electrodynamics simulator of flat band physics in a Lieb lattice. *Phys.Rev.A* **2016**, *93*, 062319.
(231) Chen, R.; Zhou, B. Finite size effects on the helical edge states on the Lieb lattice. *Chin. Phys. B* **2016**, *25*, 067204.
(232) Kock, T.; Hippler, C.; Ewerbeck, A.; Hemmerich, A. Orbital optical lattices with bosons. *Journal of Physics B-Atomic Molecular and Optical Physics* **2016**, *49*, 042001.
(233) Milicevic, M.; et al. Orbital Edge States in a Photonic Honeycomb Lattice. *Phys. Rev. Lett.* **2017**, *118*, 107403.
(234) Slot, M. R.; et al. p-Band Engineering in Artificial Electronic Lattices. *Physical Review X* **2019**, *9*, 011009.
(235) Castro Neto, A. H.; Guinea, F.; Peres, N. M. R.; Novoselov, K. S.; Geim, A. K. The electronic properties of graphene. *Rev. Mod. Phys.* **2009**, *81*, 109−162.
(236) Wu, C. J.; Das Sarma, S. px,y-orbital counterpart of graphene: Cold atoms in the honeycomb optical lattice. *Phys. Rev. B* **2008**, *77*, 235107.
(237) Wunsch, B.; Guinea, F.; Sols, F. Dirac-point engineering and topological phase transitions in honeycomb optical lattices. *New J. Phys.* **2008**, *10*, 103027.
(238) Muller, T.; Folling, S.; Widera, A.; Bloch, I. State preparation and dynamics of ultracold atoms in higher lattice orbitals. *Phys. Rev. Lett.* **2007**, *99*, 200405.
(239) Lalmi, B.; et al. Epitaxial growth of a silicene sheet. *Appl. Phys. Lett.* **2010**, *97*, 223109.
(240) Houssa, M.; et al. Electronic properties of hydrogenated silicene and germanene. *Appl. Phys. Lett.* **2011**, *98*, 223107.
(241) Liu, C.-C.; Feng, W.; Yao, Y. Quantum Spin Hall Effect in Silicene and Two-Dimensional Germanium. *Phys. Rev. Lett.* **2011**, *107*, 076802.
(242) Vogt, P.; et al. Silicene: Compelling Experimental Evidence for Graphenelike Two-Dimensional Silicon. *Phys. Rev. Lett.* **2012**, *108*, 155501.
(243) Matthes, L.; Pulci, O.; Bechstedt, F. Optical properties of two-dimensional honeycomb crystals graphene, silicene, germanene, and tinene from first principles. *New J. Phys.* **2014**, *16*, 105007.
(244) Lew Yan Voon, L. C.; Zhu, J.; Schwingenschlogl, U. Silicene: Recent theoretical advances. *Appl. Phys. Rev.* **2016**, *3*, 040802.
(245) Acun, A.; et al. Germanene: the germanium analogue of graphene. *J. Phys.-Condes. Matter* **2015**, *27*, 443002.
(246) Zhang, L.; Bampoulis, P.; van Houselt, A.; Zandvliet, H. J. W. Two-dimensional Dirac signature of germanene. *Appl. Phys. Lett.* **2015**, *107*, 111605.
(247) Post, L. C.; et al. Triangular nanoperforation and band engineering of InGaAs quantum wells: a lithographic route toward Dirac cones in III-V semiconductors. *Nanotechnology* **2019**, *30*, 155301.
(248) Park, C.-H.; Louie, S. G. Making Massless Dirac Fermions from a Patterned Two-Dimensional Electron Gas. *Nano Lett.* **2009**, *9*, 1793−1797.
(249) Nadvornik, L.; et al. From laterally modulated two-dimensional electron gas towards artificial graphene. *New J. Phys.* **2012**, *14*, 053002.
(250) De Simoni, G.; et al. Delocalized-localized transition in a semiconductor two-dimensional honeycomb lattice. *Appl. Phys. Lett.* **2010**, *97*, 132113.
(251) Wang, S.; et al. Observation of electron states of small period artificial graphene in nano-patterned GaAs quantum wells. *Appl. Phys. Lett.* **2016**, *109*, 113101.
(252) Delerue, C. Prediction of robust two-dimensional topological insulators based on Ge/Si nanotechnology. *Phys. Rev. B* **2014**, *90*, 075424.
(253) Delerue, C.; Vanmaekelbergh, D. Electronic band structure of zinc blende CdSe and rock salt PbSe semiconductors with silicene-type honeycomb geometry. *2d Materials* **2015**, *2*, 034008.
(254) Tadjine, A.; Delerue, C. Colloidal nanocrystals as LEGO (R) bricks for building electronic band structure models. *Phys. Chem. Chem. Phys.* **2018**, *20*, 8177−8184.
(255) Evers, W. H.; et al. Low-Dimensional Semiconductor Superlattices Formed by Geometric Control over Nanocrystal Attachment. *Nano Lett.* **2013**, *13*, 2317−2323.


https://doi.org/10.1021/acsnanoscienceau.1c00054
*ACS Nanosci. Au* 2022, 2, 198−224

(256) Boneschanscher, M. P.; et al. Long-range orientation and atomic attachment of nanocrystals in 2D honeycomb superlattices. *Science* **2014**, *344*, 1377−1380.
(257) Evers, W. H.; et al. High charge mobility in two-dimensional percolative networks of PbSe quantum dots connected by atomic bonds. *Nat. Commun.* **2015**, *6*, 8195.
(258) Peters, J. L.; et al. Mono- and Multilayer Silicene-Type Honeycomb Lattices by Oriented Attachment of PbSe Nanocrystals: Synthesis, Structural Characterization, and Analysis of the Disorder. *Chem. Mater.* **2018**, *30*, 4831−4837.
(259) van Overbeek, C.; et al. Interfacial Self-Assembly and Oriented Attachment in the Family of PbX (X = S, Se, Te). *Nanocrystals. J. Phys. Chem. C* **2018**, *122*, 12464−12473.
(260) Gardenier, T. S.; et al. p Orbital Flat Band and Dirac Cone in the Electronic Honeycomb Lattice. *ACS Nano* **2020**, *14*, 13638−13644.
(261) Alimoradi Jazi, M.; et al. Transport Properties of a Two-Dimensional PbSe Square Superstructure in an Electrolyte-Gated Transistor. *Nano Lett.* **2017**, *17*, 5238−5243.
(262) Franchina Vergel, N. A. Engineering a Robust Flat Band in III-V Semiconductor Heterostructures. *Nano Lett.* **2021**, *21*, 680−685.
(263) Singha, A.; et al. Correlated Electrons in Optically Tunable Quantum Dots: Building an Electron Dimer Molecule. *Phys. Rev. Lett.* **2010**, *104*, 246802.
(264) Su, W. P.; Schrieffer, J. R.; Heeger, A. J. SOLITONS IN POLYACETYLENE. *Phys. Rev. Lett.* **1979**, *42*, 1698−1701.
(265) Heeger, A. J.; Kivelson, S.; Schrieffer, J. R.; Su, W. P. SOLITONS IN CONDUCTING POLYMERS. *Rev. Mod. Phys.* **1988**, *60*, 781−850.
(266) Cheon, S.; Kim, T. H.; Lee, S. H.; Yeom, H. W. Chiral solitons in a coupled double Peierls chain. *Science* **2015**, *350*, 182−185.
(267) Groning, O.; et al. Engineering of robust topological quantum phases in graphene nanoribbons. *Nature* **2018**, *560*, 209.
(268) Rizzo, D. J.; et al. Topological band engineering of graphene nanoribbons. *Nature* **2018**, *560*, 204.
(269) Jin, K.-H.; Liu, F. 1D topological phases in transition-metal monochalcogenide nanowires. *Nanoscale* **2020**, *12*, 14661−14667.
(270) Yan, L.; Liljeroth, P. Engineered electronic states in atomically precise artificial lattices and graphene nanoribbons. *Advances in Physics-X* **2019**, *4*, 1651672.
(271) Huda, M. N.; Kezilebieke, S.; Ojanen, T.; Drost, R.; Liljeroth, P. Tuneable topological domain wall states in engineered atomic chains. *Npj Quantum Materials* **2020**, *5*, 17.
(272) Kempkes, S. N.; et al. Robust zero-energy modes in an electronic higher-order topological insulator. *Nat. Mater.* **2019**, *18*, 1292.
(273) Ezawa, M. Higher-Order Topological Insulators and Semimetals on the Breathing Kagome and Pyrochlore Lattices. *Phys. Rev. Lett.* **2018**, *120*, 026801.
(274) Benalcazar, W. A.; Bernevig, B. A.; Hughes, T. L. Quantized electric multipole insulators. *Science* **2017**, *357*, 61−66.
(275) Benalcazar, W. A.; Bernevig, B. A.; Hughes, T. L. Electric multipole moments, topological multipole moment pumping, and chiral hinge states in crystalline insulators. *Phys. Rev. B* **2017**, *96*, 245115.
(276) Benalcazar, W. A.; Li, T. H.; Hughes, T. L. Quantization of fractional corner charge in C-n-symmetric higher-order topological crystalline insulators. *Phys. Rev. B* **2019**, *99*, 245151.
(277) Schindler, F. Higher-order topological insulators. *Science Advances* **2018**, *4*, eaat0346.
(278) Schindler, F.; et al. Higher-order topology in bismuth. *Nat. Phys.* **2018**, *14*, 918.
(279) Noh, J.; et al. Topological protection of photonic mid-gap defect modes. *Nat. Photonics* **2018**, *12*, 408−415.
(280) Serra-Garcia, M.; et al. Observation of a phononic quadrupole topological insulator. *Nature* **2018**, *555*, 342.
(281) Peterson, C. W.; Benalcazar, W. A.; Hughes, T. L.; Bahl, G. A quantized microwave quadrupole insulator with topologically protected corner states. *Nature* **2018**, *555*, 346.
(282) Imhof, S.; et al. Topolectrical-circuit realization of topological corner modes. *Nat. Phys.* **2018**, *14*, 925.
(283) Ni, X.; Weiner, M.; Alu, A.; Khanikaev, A. B. Observation of higher-order topological acoustic states protected by generalized chiral symmetry. *Nat. Mater.* **2019**, *18*, 113.
(284) Li, M.; et al. Higher-order topological states in photonic kagome crystals with long-range interactions. *Nat. Photonics* **2020**, *14*, 89.
(285) van Miert, G.; Ortix, C. On the topological immunity of corner states in two-dimensional crystalline insulators. *Npj Quantum Materials* **2020**, *5*, 63.
(286) Proctor, M.; Blanco de Paz, M.; Bercioux, D.; Garcia-Etxarri, A.; Huidobro, P. A. Higher-order topology in plasmonic Kagome lattices. *Appl. Phys. Lett.* **2021**, *118*, 091105.
(287) Fu, L. Topological Crystalline Insulators. *Phys. Rev. Lett.* **2011**, *106*, 106802.
(288) Freeney, S. E.; van den Broeke, J. J.; van Der Veen, A.; Swart, I.; Smith, C. M. Edge-Dependent Topology in Kekule Lattices. *Phys. Rev. Lett.* **2020**, *124*, 236404.
(289) Xie, B. Y.; et al. Acoustic Topological Transport and Refraction in a Kekule Lattice. *Physical Review Applied* **2019**, *11*, 044086.
(290) Wu, L. H.; Hu, X. Topological Properties of Electrons in Honeycomb Lattice with Detuned Hopping Energy. *Sci. Rep* **2016**, *6*, 24347.
(291) Kariyado, T.; Hu, X. Topological States Characterized by Mirror Winding Numbers in Graphene with Bond Modulation. *Sci. Rep* **2017**, *7*, 41598.
(292) Nadj-Perge, S.; et al. Observation of Majorana fermions in ferromagnetic atomic chains on a superconductor. *Science* **2014**, *346*, 602−607.
(293) Pawlak, R.; et al. Probing atomic structure and Majorana wavefunctions in mono-atomic Fe chains on superconducting Pb surface. *Npj Quantum Information* **2016**, *2*, 16035.
(294) Jeon, S.; et al. Distinguishing a Majorana zero mode using spin-resolved measurements. *Science* **2017**, *358*, 772.
(295) Kim, H.; et al. Toward tailoring Majorana bound states in artificially constructed magnetic atom chains on elemental superconductors. *Science Advances* **2018**, *4*, 5251.
(296) Schneider, L.; et al. Controlling in-gap end states by linking nonmagnetic atoms and artificially-constructed spin chains on superconductors. *Nat. Commun.* **2020**, *11*, 4707.
(297) Groning, O.; et al. Engineering of robust topological quantum phases in graphene nanoribbons. *Nature* **2018**, *560*, 209.
(298) Shechtman, D.; Blech, I.; Gratias, D.; Cahn, J. W. METALLIC PHASE WITH LONG-RANGE ORIENTATIONAL ORDER AND NO TRANSLATIONAL SYMMETRY. *Phys. Rev. Lett.* **1984**, *53*, 1951.
(299) Talapin, D. V.; et al. Quasicrystalline order in self-assembled binary nanoparticle superlattices. *Nature* **2009**, *461*, 964−967.
(300) Wang, D.; et al. Binary icosahedral clusters of hard spheres in spherical confinement. *Nat. Phys.* **2021**, *17*, 128.
(301) Shang, J.; et al. Assembling molecular Sierpinski triangle fractals. *Nat. Chem.* **2015**, *7*, 389−393.
(302) Zhang, X.; et al. Robust Sierpinski triangle fractals on symmetry-mismatched Ag(100). *Chem. Commun.* **2016**, *52*, 10578−10581.
(303) Shechtman, D.; Blech, I. A. THE MICROSTRUCTURE OF RAPIDLY SOLIDIFIED AL6MN. *Metallurgical Transactions a-Physical Metallurgy and Materials Science* **1985**, *16*, 1005−1012.
(304) Lipsitt, H. A.; Shechtman, D.; Schafrik, R. E. DEFORMATION AND FRACTURE OF TIAL AT ELEVATED-TEMPERATURES. *Metallurgical Transactions a-Physical Metallurgy and Materials Science* **1975**, *6*, 1991−1996.
(305) Lin, C.; et al. Evidence of cross-cutting and redox reaction in Khatyrka meteorite reveals metallic-Al minerals formed in outer space. *Sci. Rep* **2017**, *7*, 1637.


https://doi.org/10.1021/acsnanoscienceau.1c00054
*ACS Nanosci. Au* 2022, 2, 198−224

(306) Gopalakrishnan, S.; Martin, I.; Demler, E. A. Quantum Quasicrystals of Spin-Orbit-Coupled Dipolar Bosons. *Phys. Rev. Lett.* **2013**, *111*, 185304.
(307) Jagannathan, A.; Duneau, M. An eightfold optical quasicrystal with cold atoms. *Epl* **2013**, *104*, 66003.
(308) Vardeny, Z. V.; Nahata, A.; Agrawal, A. Optics of photonic quasicrystals. *Nat. Photonics* **2013**, *7*, 177−187.
(309) Collins, L. C.; Witte, T. G.; Silverman, R.; Green, D. B.; Gomes, K. K. Imaging quasiperiodic electronic states in a synthetic Penrose tiling. *Nat. Commun.* **2017**, *8*, 15961.
(310) Schwalm, W. A.; Schwalm, M. K. ELECTRONIC-PROPERTIES OF FRACTAL-GLASS MODELS. *Phys. Rev. B* **1989**, *39*, 12872.
(311) Devries, P.; Deraedt, H.; Lagendijk, A. WAVE LOCALIZATION IN DISORDERED AND FRACTAL SYSTEMS. *Comput. Phys. Commun.* **1993**, *75*, 298−310.
(312) Aharony, A.; Harris, A. B. SUPERLOCALIZATION OF WAVE-FUNCTIONS ON FRACTAL NETWORKS. *Physica A* **1994**, *205*, 335−341.
(313) Chakrabarti, A. Exact results for infinite and finite Sierpinski gasket fractals: Extended electron states and transmission properties. *J. Phys.-Condes. Matter* **1996**, *8*, 10951−10957.
(314) Chuprikov, N. L.; Spiridonova, O. V. A new type of solution of the Schrodinger equation on a self-similar fractal potential. *J. Phys. A: Math. Gen.* **2006**, *39*, L559−L562.
(315) Bercioux, D.; Iñiguez, A. Quantum fractals. *Nat. Phys.* **2019**, *15*, 111−112.
(316) Gu, G. C.; et al. Sierpiriski Triangle Fractal Structures Investigated by STM. *Acta Phys.-Chim. Sin.* **2016**, *32*, 195−200.
(317) Kempkes, S. N.; et al. Design and characterization of electrons in a fractal geometry. *Nat. Phys.* **2019**, *15*, 127.
(318) Feigel'man, M. V.; Ioffe, L. B.; Kravtsov, V. E.; Cuevas, E. Fractal superconductivity near localization threshold. *Annals of Physics* **2010**, *325*, 1390−1478.
(319) Markos, P.; Schweitzer, L. Critical regime of two-dimensional Ando model: relation between critical conductance and fractal dimension of electronic eigenstates. *Journal of Physics a-Mathematical and General* **2006**, *39*, 3221−3230.
(320) Vanmaekelbergh, D.; Liljeroth, P. Electron-conducting quantum dot solids: novel materials based on colloidal semiconductor nanocrystals. *Chem. Soc. Rev.* **2005**, *34*, 299−312.
(321) Buth, F.; Donner, A.; Sachsenhauser, M.; Stutzmann, M.; Garrido, J. A. Biofunctional Electrolyte-Gated Organic Field-Effect Transistors. *Adv. Mater.* **2012**, *24*, 4511−4517.
(322) Huijben, M.; et al. Structure-Property Relation of SrTiO3/LaAlO3 Interfaces. *Adv. Mater.* **2009**, *21*, 1665−1677.
(323) Neyens, S. F.; et al. The critical role of substrate disorder in valley splitting in Si quantum wells. *Appl. Phys. Lett.* **2018**, *112*, 243107.
(324) Klitzing, K. v.; Dorda, G.; Pepper, M. NEW METHOD FOR HIGH-ACCURACY DETERMINATION OF THE FINE-STRUCTURE CONSTANT BASED ON QUANTIZED HALL RESISTANCE. *Phys. Rev. Lett.* **1980**, *45*, 494−497.
(325) Halperin, B. I. QUANTIZED HALL CONDUCTANCE, CURRENT-CARRYING EDGE STATES, AND THE EXISTENCE OF EXTENDED STATES IN A TWO-DIMENSIONAL DISORDERED POTENTIAL. *Phys. Rev. B* **1982**, *25*, 2185−2190.
(326) Halperin, B. I. THEORY OF THE QUANTIZED HALL CONDUCTANCE. *Helv. Phys. Acta* **1983**, *56*, 75−102.
(327) Du, R. R.; Tsui, D. C.; Stormer, H. L.; Pfeiffer, L. N.; West, K. W. EXPERIMENTAL-EVIDENCE FOR COMPOSITE-PARTICLES IN THE FRACTIONAL QUANTUM HALL-EFFECT. *Surf. Sci.* **1994**, *305*, 18−22.
(328) Laughlin, R. B. ANOMALOUS QUANTUM HALL-EFFECT - AN INCOMPRESSIBLE QUANTUM FLUID WITH FRACTIONALLY CHARGED EXCITATIONS. *Phys. Rev. Lett.* **1983**, *50*, 1395−1398.
(329) Halperin, B. I. STATISTICS OF QUASIPARTICLES AND THE HIERARCHY OF FRACTIONAL QUANTIZED HALL STATES. *Phys. Rev. Lett.* **1984**, *52*, 1583−1586.
(330) Wallace, P. R. THE BAND THEORY OF GRAPHITE. *Phys. Rev.* **1947**, *71*, 622−634.
(331) Sorella, S.; Tosatti, E. SEMIMETAL INSULATOR TRANSITION OF THE HUBBARD-MODEL IN THE HONEYCOMB LATTICE. *Europhys. Lett.* **1992**, *19*, 699−704.
(332) Gonzalez, J.; Guinea, F.; Vozmediano, M. A. H. NON-FERMI LIQUID BEHAVIOR OF ELECTRONS IN THE HALF-FILLED HONEYCOMB LATTICE - (A RENORMALIZATION-GROUP APPROACH). *Nucl. Phys. B* **1994**, *424*, 595−618.
(333) Paiva, T.; Scalettar, R. T.; Zheng, W.; Singh, R. R. P.; Oitmaa, J. Ground-state and finite-temperature signatures of quantum phase transitions in the half-filled Hubbard model on a honeycomb lattice. *Phys. Rev. B* **2005**, *72*, 085123.
(334) Herbut, I. F. Interactions and phase transitions on graphene's honeycomb lattice. *Phys. Rev. Lett.* **2006**, *97*, 146401.
(335) Herbut, I. F.; Juricic, V.; Roy, B. Theory of interacting electrons on the honeycomb lattice. *Phys. Rev. B* **2009**, *79*, 085116.
(336) Ando, T.; Zheng, Y. S.; Suzuura, H. Dynamical conductivity and zero-mode anomaly in honeycomb lattices. *J. Phys. Soc. Jpn.* **2002**, *71*, 1318.
(337) Park, C.-H.; Yang, L.; Son, Y.-W.; Cohen, M. L.; Louie, S. G. New generation of massless Dirac fermions in graphene under external periodic potentials. *Phys. Rev. Lett.* **2008**, *101*, 126804.
(338) Hasegawa, Y.; Konno, R.; Nakano, H.; Kohmoto, M. Zero modes of tight-binding electrons on the honeycomb lattice. *Phys. Rev. B* **2006**, *74*, 033413.
(339) Tadjine, A.; Allan, G.; Delerue, C. From lattice Hamiltonians to tunable band structures by lithographic design. *Phys. Rev. B* **2016**, *94*, 075441.
(340) Soibel, A.; Meirav, U.; Mahalu, D.; Shtrikman, H. Fabrication and transport measurements of honeycomb surface superlattices. *Semicond. Sci. Technol.* **1996**, *11*, 1756−1760.
(341) Binnig, G.; Rohrer, H. In touch with atoms. *Rev. Mod. Phys.* **1999**, *71*, S324.
(342) Crommie, M. F.; Lutz, C. P.; Eigler, D. Confinement of Electrons to Quantum Corrals on a Metal. *Science* **1993**, *262*, 218.
(343) Freeney, S. E.; Borman, S. T. P.; Harteveld, J. W.; Swart, I. Coupling quantum corrals to form artificial molecules. *SciPost Phys.* **2020**, *9*, 085.
(344) Trainer, D. J. et al. Manipulating topology in tailored artificial graphene nanoribbons. *arXiv (Mesoscale and Nanoscale)*, April 22, **2021**, 2104.11334, ver. 1.


https://doi.org/10.1021/acsnanoscienceau.1c00054
*ACS Nanosci. Au* 2022, 2, 198−224